A New Perspective on Magnetotail Electron and Ion Divergent Flows: MMS Observations

T. Motoba[1], M. I. Sitnov[1], G. K. Stephens[1], and D. J. Gershman[2]

1. The Johns Hopkins University Applied Physics Laboratory, Laurel, MD, USA
2. NASA Goddard Space Flight Center, Greenbelt, MD, USA

Key points:

- Transient electron flow reversals embedded into a more gradual ion flow reversal in the magnetotail occur without magnetic topology change
- Properties of the discovered divergent flows are distinctly different from those of reconnection outflows in the electron diffusion region
- Divergent flows are interpreted as flow-driven reconnection onsets due to the ion tearing or the ballooning/interchange instability

Corresponding author:
Tetsuo Motoba, (tetsuo.motoba@gmail.com)

Update: August 17, 2022

Abstract.

Fast divergent flows of electrons and ions in the magnetotail plasma sheet are conventionally interpreted as a key reconnection signature caused by the magnetic topology change at the X-line. Therefore, reversals of the x-component ($V_{x\perp}$) of the plasma flow perpendicular to the magnetic field must correlate with the sign changes in the north-south component of the magnetic field (B_z). Here we present observations of the flow reversals that take place with no correlated B_z reversals. We report six such events, which were measured with the high-resolution plasma and fields instruments of the Magnetospheric Multiscale (MMS) mission. We found that electron flow reversals in the absence of B_z reversals (1) have amplitudes of ~1,000–2,000 km s^{-1} and durations of a few seconds; (2) are embedded into larger-scale ion flow reversals with enhanced ion agyrotropy; and (3) compared with conventional reconnection outflows around the electron diffusion regions (EDRs), have less (if ever) pronounced electron agyrotropy, dawnward electron flow amplitude, and electric field strength toward the neutral sheet, although their energy conversion parameters, including the Joule heating rate, are quite substantial. These results suggest that such flow reversals develop in the ion-demagnetization regions away from electron-scale current sheets, in particular the EDRs, and yet they play an important role in the energy conversion. These divergent flows are interpreted as precursors of the flow-driven reconnection onsets provided by the ion tearing or the ballooning/interchange instability.

1. Introduction

Magnetic reconnection is a key process in collisionless plasmas that converts magnetic energy into plasma kinetic and thermal energies through a rapid change of magnetic field topology. At the Earth's magnetopause, the reconnection process leads to efficient transport of solar wind energy into the magnetosphere, whereas in the magnetotail, it explosively releases the accumulated magnetic energy and causes global geomagnetic disturbances leading to auroral substorms (Hones, 1984; Baker et al., 1996). The energy conversion and topological changes take place in a very small region surrounding an X-line where ions or both ions and electrons are decoupled from the magnetic field. These regions are called the diffusion regions. They have a multiscale structure due to different masses and hence dynamics of ions and electrons. A larger ion diffusion region (IDR) with unmagnetized ions usually contains a smaller-scale electron diffusion region (EDR) where both electrons and ions are unmagnetized.

A distinctive feature of the magnetotail reconnection onset is that corresponding plasma motions are needed to reduce the original finite normal magnetic field for the formation of an X-line. This is not necessary in case of antiparallel or sheared magnetic field configurations, such as at the magnetopause. Indeed, there is some controversy regarding whether fast plasma divergent flows in the magnetotail are a consequence or a cause of the magnetic topology change. In the former and the most commonly accepted scenario, the magnetic topology first changes because of the slow evolution of the tail induced by the external driving and subsequent microscale tearing instability (e.g., Liu et al., 2014). Therefore, plasma divergent flows arise from the unbalanced magnetic tension of the sharply

kinked, newly reconnected field lines around the X-line.

The latter scenario was originally proposed by Lin and Swift (2002). On the basis of the analysis of their 2-D global hybrid simulations, they conjectured that the magnetic topology change can be internally driven by the spontaneous generation of plasma divergent flows. The idea of such flows preceding and likely driving the reconnection onset was later elaborated on by Siscoe et al. (2009) and Tanaka et al. (2019) in the analysis of their magnetohydrodynamic (MHD) simulations. These plasma divergent flows are referred to below as plasma "watersheds" (WSs), to distinguish them from reconnection ejecta emanated from an already formed X-line. Most recently, Sitnov et al. (2021a), using fully kinetic 3-D particle-in-cell (PIC) simulations, discovered that the preonset diverging flows have a complex structure with multiple electron WSs being embedded into a larger-scale ion WS. Although they also provided an example of WS-like structures from the Magnetospheric Multiscale (MMS) observations in the magnetotail to compare them with the PIC simulation results, the measurements could be mixed with the regimes of electron-only or guide-field reconnection (Phan et al., 2018; Chen et al., 2019). Thus, the primary objective of this study is to conduct a detailed multicase investigation of electron and ion WSs in the magnetotail using capabilities of MMS instruments and to determine the distinctive features of WSs.

When a spacecraft is crossing the diffusion regions along the outflow direction in the vicinity of an X-line, the expected signatures would be a reversal of earthward and tailward convective flows (i.e., $V_{x\perp}$, perpendicular to the magnetic field in the Geocentric Solar Magnetospheric [GSM] coordinate system) as well as a reversal of the northward component of the magnetic field (B_z in GSM). Indeed, such $V_{x\perp}$ and B_z (or $V_{L\perp}$ and B_N in the local

coordinate system (so-called "LMN"), where **L** is in the outflow direction (roughly sunward in the magnetotail), **M** along the X-line (roughly duskward), and **N** normal to the current sheet (roughly northward)) reversals have been detected in magnetotail observations made by Wind (Øieroset et al., 2001), Geotail (Nagai et al., 2011), Cluster (Runov et al., 2003), THEMIS (Angelopoulos et al., 2020), and MMS (Torbert et al., 2018). Moreover, the collisionless nature of reconnection has been confirmed by observed signatures of the Hall fields, the bipolar electric field E_z in GSM (or E_N in LMN) toward the neutral plane, and the quadrupolar out-of-plane magnetic field B_y in GSM (or B_M in LMN) (e.g., Eastwood et al. 2010a, 2010b).

The unprecedented time and space resolution of the MMS mission allows one to further investigate different regimes of the magnetotail reconnection and its onset details. In this paper, we seek to observationally characterize kinetic field and plasma features of ion and electron WSs in the magnetotail using MMS data, emphasizing how these features contrast with those of conventional reconnection ejecta from the EDR (Torbert et al., 2018) as well as divergent electron flows in electron-only reconnection regimes (Phan et al., 2018).

The remainder of this study is organized as follows. Section 2 describes the instrumentation and data. Section 3.1 briefly describes the key features of the "benchmark" 11 July 2017 EDR event observed in the magnetotail. In section 3.2, we first describe the event selection and then present three representative WS events (Events 1–3) by comparing them with the 11 July 2017 EDR event as well as with simulation results of the flow-driven magnetotail reconnection regimes. In addition, we briefly introduce three other WS events (Events 4–6) that took place in more dipolarized tail regions and compare them with Events

1–3. Section 4 summarizes the results and discusses their implications.

2. Data and Instrumentation

MMS (Burch et al., 2016) is composed of four identical spacecraft that were launched in March 2015, to investigate small-scale reconnection physics in the Earth's magnetosphere, particularly the electron-scale physics. In this study, we utilize the fast survey and burst mode data of fields and plasma moments acquired from the FIELDS (Torbert et al., 2016) and Fast Plasma Investigation (FPI; Pollock et al., 2016) instruments on board MMS; burst-mode (128 Hz) magnetic field vector (**B**) data measured by the FIELDS Flux Gate Magnetometer (FGM; Russell et al., 2016); fast survey-mode (32 Hz) electric field vector (**E**) data measured by the Electric field Double Probes (EDP; Ergun et al., 2016; Lindqvist et al., 2016); and burst-mode ion (150 ms) and electron (30 ms) moment data at 0.01–30.0 keV/q measured by FPI.

The burst-mode FPI plasma moment data enable us to directly estimate two important parameters that characterize WSs. One is the current density (**J**): $\mathbf{J} = qN_e(\mathbf{V_i} - \mathbf{V_e})$, where q is the elementary charge, N_e is the electron density (assuming quasi-neutrality), $\mathbf{V_i}$ is the ion bulk velocity, and $\mathbf{V_e}$ is the electron bulk velocity. Another is the so-called Q-parameter (Swisdak, 2016), which is a scalar measure of agyrotropy (non-gyrotropy) of plasma species that reflects the degree of demagnetization of electrons and ions (mainly protons). The Q-parameter can be calculated from the following equation (its square-root value is discussed in the literature): $Q_\alpha^{1/2} = [(P_\alpha{}^2{}_{12} + P_\alpha{}^2{}_{13} + P_\alpha{}^2{}_{23})/(P_\alpha{}^2{}_\perp + 2\, P_\alpha{}^2{}_\perp\, P_\alpha{}^2{}_\parallel)]^{1/2}$, where α is species.

Here, $Q^{1/2} = 0$ ($Q^{1/2} = 1$) means that plasma tends to be gyrotropic (agyrotropic).

3. Observations

3.1. EDR on 11 July 2017

Here let us briefly summarize key features of the magnetotail EDR event on 11 July 2017, which was originally reported by Torbert et al. (2018; hereafter referred to as "T18"), in order to differentiate the plasma WSs presented in section 3.2 from this classical magnetotail reconnection picture. Figure 1 shows an overview plot of MMS 3 field and plasma measurements for a 30-s interval of 2233:45–2234:15 UT on 11 July 2017 to characterize the magnetotail EDR. These parameters are displayed in the GSM coordinate system – instead of the LMN coordinate system used in T18 – because for this EDR event, the GSM coordinate system is close to the LMN coordinate system (i.e., $x \sim L$, $y \sim M$, and $z \sim N$), as reported by Genestreti et al. (2018) using various methods. We also note that MMS data are shown in the GSM coordinate system throughout the paper, unless otherwise specified.

When MMS 3 encountered the EDR at approximately 2234:03 UT (vertical dashed line), the spacecraft stayed close to the magnetotail central plasma sheet (CPS) at a radial distance of ~22 R_E, where $|B|$ and plasma density (N_e and N_i) decreased to a minimum of ~1 nT (Figure 1a) and ~0.03–0.05 cm^{-3} (Figure 1d), respectively, whereas the plasma beta (β, the ratio of the magnetic and plasma pressures) reached a pronounced peak of ~ 800 (Figure 1e).

The EDR properties extracted from the MMS 3 observations, which are key points for

144 the subsequent comparison with WS observations, can be summarized as follows: (1) the x
145 components of the perpendicular ion and electron flows, $V_{ix\perp}$ and $V_{ex\perp}$, exhibit simultaneous
146 tailward-to-earthward reversals in the high-β region (Figures 1b, 1c, and 1e); (2) the flow
147 reversals are accompanied by a negative-to-positive sign change in B_z (Figure 1a) and a
148 minimum in plasma density (Figure 1d); (3) the perpendicular electron velocity, $V_{ex\perp}$,
149 generally follows $(E\times B)_x/|B|^2$ in the divergent jets (Figure 1c); (4) the dawnward electron
150 velocity component is super-Alfvénic ($V_{eM} \approx -15{,}000$ km s^{-1} in LMN; not shown here, but
151 see Figure 2C of T18); (5) electron agyrotropy, $Q_e^{1/2}$, exhibits a short-lived enhancement of
152 ~0.25 in the vicinity of the $V_{ex\perp}$ reversal (Figure 1f); and (6) ion agyrotropy, $Q_i^{1/2}$, is elevated
153 by ~0.2–0.4 for a much longer interval (Figure 1f).

154 Deviations of $V_{ex\perp}$ from $(E\times B)_x/|B|^2$ (particularly in the earthward flow region) and $Q_e^{1/2}$
155 enhancement provide strong evidence that electrons are demagnetized in the vicinity of the
156 EDR. Furthermore, different temporal variations of the $Q_e^{1/2}$ and $Q_i^{1/2}$ enhancements reveal
157 a multiscale structure of the reconnection diffusion region with a smaller-scale EDR being
158 embedded into a larger-scale IDR. It is worth noting that $\mathbf{J}\cdot\mathbf{E}' = \mathbf{J}\cdot(\mathbf{E}+\mathbf{V_e}\times\mathbf{B})$, considered as
159 an MHD measure of the Joule dissipation (Birn and Hesse, 2005; Zenitani et al., 2011),
160 becomes positive with a peak value of ~0.3 nW m^{-3} in the vicinity of the $V_{ex\perp}$ reversal and
161 that the normal component of the electric field E_N in LMN (directed toward the neutral plane)
162 has a Hall-related bipolar signature on the order of several tens of mV m^{-1}, as seen in Figures
163 2H and 2G of T18. Overall, the high-resolution MMS observations have revealed the
164 theoretically-predicted properties of the EDR, including the concurrent $V_{ex\perp}$, $V_{ix\perp}$ and B_z
165 reversals, a dawnward super-Alfvénic electron jet, electron demagnetization ($V_{ex\perp} \neq$

166 $(E\times B)_x/|B|^2$), $Q_e^{1/2}$ enhancement, strong variations of the Joule heating rate $\mathbf{J}\cdot\mathbf{E}'$, and a strong
167 Hall electric field toward the neutral plane.

168 In section 3.2 we will highlight the main properties of electron and ion WSs in the
169 magnetotail by comparing them with the key properties of the T18 EDR event described
170 above.

171

172 **3.2. Plasma WSs**

173 In recent PIC simulations, Sitnov et al. (2021a) have provided a number of distinctive
174 features of ion and electron WSs in the magnetotail at the kinetic level of their description.
175 First, electron and ion WSs occur on different spatial and temporal scales: an electron WS
176 has a transient, small-scale structure compared with a more sustained, larger-scale ion WS.
177 Second, small-scale electron WSs are embedded into a larger-scale ion WS. Third, in the WS
178 region, ions are mostly demagnetized, whereas electrons are mostly magnetized. Fourth, and
179 most importantly, an electron WS is not accompanied by the concurrent magnetic topology
180 change, unlike the EDR. (Note that Sitnov et al. (2021a) also found regimes with ion WSs,
181 when the divergent ion flows occur in the absence of the magnetic topology change. However,
182 because MMS provides electron-scale resolution, these ion-scale effects are not in the focus
183 of our study.) On the basis of such expected properties, we selected six potential WS
184 candidates by visually inspecting the MMS quick-look burst plots
185 (https://lasp.colorado.edu/mms/sdc/public/) during the 2017–2020 tail phases. All the
186 selected events meet the following criteria: (1) transient reversals of the electron flow

187 perpendicular to the magnetic field ($V_{ex\perp}$) occur in either the earthward or tailward flow
188 region of a single ion flow reversal ($V_{ix\perp}$); (2) the transient $V_{ex\perp}$ reversals occur in the absence
189 of B_z reversals; (3) MMS probes are located in a CPS region of the magnetotail with plasma
190 $\beta > 1$ (cf. Baumjohann et al., 1989); and (4) the plasma density during WS crossings is greater
191 than 0.1 cm^{-3}. The last criterion guarantees a certain level of FPI moment data quality.

192 In sections 3.2.1–3.2.3, we first describe each of three representative WS events (Events
193 1–3) that appear to be most closely similar to the WS simulations by Sitnov et al. (2021a)
194 and a manifestation of the flow-driven reconnection. In section 3.2.4, we briefly describe
195 three other WSs (Events 4–6) that occurred under stronger B_z conditions and are interpreted
196 in terms of a mechanism different from that of Events 1–3. Data analysis is largely limited to
197 the MMS 1 observations in the GSM coordinate system. For the interested reader, however,
198 the key parameters at the other available MMS probes and the WS pictures in an LMN
199 coordinate system for selected events are provided in the supporting information (SI).

200

201 ### 3.2.1. 2 August 2020 Event: Event 1

202 The first WS event, Event 1, took place on 2 August 2020 when the MMS tetrahedron
203 was located at (X, Y, Z) = (–28.0, –1.8, 4.0) R_E in GSM coordinates, with an interspacecraft
204 separation of ~40 ± 5 km. Event 1 occurred under geomagnetically active conditions when
205 the z component of the interplanetary magnetic field (IMF B_z) ranged from –5 to –10 nT for
206 several hours (Figure S1 in the SI), and it was the only event in which B_z decreased to ~2 nT,

in contrast to the other five events where $B_z > 5$ nT.

Figure 2 displays MMS 1 observations of Event 1 at 1446:00–1448:30 UT. At ~1446:36 UT the x component of the perpendicular electron velocity ($V_{ex\perp}$) made a transient, earthward-to-tailward reversal (Figure 2c). The $V_{ex\perp}$ reversal time, highlighted by gray shading, is hereinafter referred to as t_r. During the transient reversal, the $V_{ex\perp}$ value varied from approximately 1,000 to –1,500 km s^{-1}. These peak values are greater than the local ion Alfvén speed (~120–300 km s^{-1}) based on $|B|$ = 4–10 nT and N_i = 0.5 cm^{-3}. Interestingly, the x component of the perpendicular ion velocity ($V_{ix\perp}$, Figure 2b) did not respond to the transient $V_{ex\perp}$ reversal at all, indicating that electrons and ions were decoupled. The transient flow reversal of electrons was embedded in a more gradual earthward-to-tailward flow reversal of ions with $|V_{ix\perp}|$ ~300 km s^{-1}, which took place at ~1447:25 UT. Hereafter these electron and ion divergent flows are referred to as electron and ion WSs, respectively.

Within the transient electron WS, the magnetic field strength, $|B|$ (Figure 2a), decreased from ~10 to ~4 nT, whereas the plasma density (N_i and N_e, Figure 2d) slightly increased from 0.4 to 0.5 cm^{-3}. As a result, the plasma β value sharply jumped from ~5 up to ~60 (Figure 2e). We also found that the electron WS appeared within an extended interval of elevated ion agyrotropy, $Q_\mathrm{i}^{1/2} \sim 0.18$ (Figure 2f). Both results indicate that the electron WS was located in a CPS region of the magnetotail where ions were unmagnetized.

On a larger scale, the ion WS at ~1447:25 UT occurred under positive values of B_z ~5–10 nT, as predicted for WS simulations. Approximately 50 s later, B_z reversal took place, suggesting that the ion-scale reversal could also be interpreted as an IDR (e.g., Rogers et al., 2019). With the present MMS probe separation, however, it is impossible to judge whether

the ion flow drove the topology change or the latter took place before the ion flow reversal but in a different region in space, which the MMS spacecraft detected later.

To further analyze the electron WS, Figure 3 presents a zoomed-in view of the field and plasma data during the 10-s interval of 1446:30–1446:40 UT, marked by two dashed vertical lines in Figure 2. Shown from top to bottom are **B** (Figure 3a); $\mathbf{V}_i$ (Figure 3b); $\mathbf{V}_e$ (Figure 3c); $V_{ex\perp}$, $V_{ix\perp}$ and $(E\times B)_x/|B|^2$ (Figure 3d); **J** (Figure 3e); **E** (Figure 3f); $T_{e\perp}$ and $T_{e||}$ (Figure 3g); $\mathbf{J}\cdot\mathbf{E}$ and $\mathbf{J}\cdot\mathbf{E}'$ (Figure 3g); and ion and electron agyrotropy, $Q_i^{1/2}$ and $Q_e^{1/2}$ (Figure 3i). A vertical dashed line is drawn at t_r = 1446:36 UT, and the gray shading represents an interval of $t_r \pm 1$ s. We also provide in Figure S2 the same parameters displayed in an LMN coordinate system. Similar to the T18 EDR event, the normal component is almost in the z direction in the GSM coordinate system.

It is important to note here that the interpretation of the Joule heating rate must be used with an extreme caution. As already shown in equation 8 of Zenitani et al. (2011), in quasi-neutral plasmas, the parameter $\mathbf{J}\cdot\mathbf{E}'$ cannot distinguish between ion and electron species. Therefore, it cannot be used as a measure of the kinetic (Landau) dissipation, which is distinctly different for different plasma species. Thus, in the analysis of collisionless dissipation in magnetic reconnection, $\mathbf{J}\cdot\mathbf{E}'$ must be replaced by the kinetic analogs based on the pressure-strain interaction (Yang et al., 2017; Sitnov et al., 2018, 2021b; Bandyopadhyay et al., 2021). At the same time, the MMS tail observations pose another challenge because of an insufficient probe spacing, which may not match the time resolution (Sitnov et al., 2021b). This is why below we have to limit our analysis by the parameters $\mathbf{J}\cdot\mathbf{E}$ and $\mathbf{J}\cdot\mathbf{E}'$.

Similar to the T18 EDR event (Figure 1a), this electron WS occurred at a minimum $|B|$

that rapidly dropped to ~4 nT (Figure 3a). However, we emphasize that most other properties of this WS are drastically different from the T18 EDR event. First, the sign of the normal magnetic field, B_z, remained unchanged (Figures 3a and 3d), suggesting the preserved tail topology during this event.

Second, the electron flow velocity reversal was not accompanied by a comparable peak in the dawnward electron velocity ($|V_{ey}| \leq |V_{ex}|$, Figure 3c) or the duskward current density ($|J_y| \leq |J_x|$, Figure 3e). This result can be contrasted with Figures 2C and 2E in T18, showing dawnward super-Alfvénic electron jets with $|V_{eM}|$ ~15,000 km s^{-1} > $|V_{eL}|$ and the corresponding strong duskward current density with $|J_M|$ ~100 nA m^{-2} > $|J_L|$.

Third, the electric field E_z normal to the neutral plane was relatively weak ($|E_z| < 2$ mV m^{-1}, Figure 3f), unlike Figure 2G in T18 indicating strong bipolar E_N, pointing toward the center of the current sheet (the Hall electric field) with $|E_N| \sim 30$ mV m^{-1}. This result, together with the second result, suggests that the electron WS region was away from electron-scale thin current sheets.

Fourth, the quantitative discrepancy between $|V_{ex\perp}|$ and $|(E\times B)_x/|B|^2|$ in the electron WS region (Figure 3d) was larger, compared with the T18 EDR event (Figure 1c). Such strong deviations of magnetized electron flows (red curve in Figure 3i) from their frozen-in motion can be explained by their Hall interaction with unmagnetized ions (black line in Figure 3i) as is the case in the ion-tearing mode (e.g., Sitnov & Swisdak, 2011).

At the same time, whereas the energy conversion rate $\mathbf{J}\cdot\mathbf{E}$ and the Joule heating rate $\mathbf{J}\cdot\mathbf{E}'$ were nearly zero at t_r (Figure 3h), ~1 s later, they had substantial positive and negative

272 excursions with amplitudes of ~0.1 nW m^{-3} comparable to those for the T18 EDR event ($\mathbf{J}\cdot\mathbf{E}'$
273 ~0.3 nW m^{-3}). This suggests that, like the EDR, this electron WS was a site of the strong
274 energy conversion, consistent with the ion-tearing mechanism (Schindler, 1974; Sitnov &
275 Swisdak, 2011; Sitnov et al., 2013).

276 To make sure that the obtained WS picture is consistent with other MMS probe
277 observations, we provide in Figure S3 an analog of Figures 3a–3c using data from all
278 available MMS probes. Note that the FPI electron and ion moment data at MMS 2 and the
279 FPI electron moment data at MMS 4 are not available in the required burst mode during
280 Event 1. It is evident from Figure S3 that the magnetic field and bulk flow velocity data at
281 all available probes are generally consistent with each other. At the same time, such a similar
282 picture makes it hard to clarify the global reconnection geometry because of much smaller
283 probe separation than missions like Cluster (Eastwood et al., 2005).

284 To further clarify the global context of Event 1, we used global reconstructions of the
285 magnetic field that have become possible because of the application of the data mining (DM)
286 technique to historical archives of multi-mission magnetometer data (Stephens et al., 2019;
287 Sitnov et al., 2019). The DM provides the geomagnetic field reconstructions with a time
288 sampling of 5 min, and the reconstructions are quantified by the SuperMAG geomagnetic
289 indices, SMR and SML (equivalent to Sym-H and AL), their time derivatives, and the solar
290 wind input parameter $V_{sw}\cdot B_s^{\mathrm{IMF}}$ (V_{sw} is the solar wind velocity and B_s^{IMF} is equivalent to IMF
291 B_z). The DM outputs for Event 1 are shown in Figure 4.

292 Figure 4a presents comparison of 5-min averaged magnetic field vectors observed at
293 MMS 1 (black curves) with the DM outputs (red curves) for the interval of 1100–1500 UT.

The DM outputs represent magnetic field vectors reconstructed along the MMS 1 orbit. The moment closest to the WS observations at MMS (1445 UT) is marked by the dashed vertical line. Throughout the interval, the DM output generally follows the observed magnetic field variations, although there are some exceptions, particularly for the x- and y-components. Such a good agreement between the observed and reconstructed magnetic fields at MMS 1 guarantees a certain level of DM output reliability.

Figure 4b shows the distribution of B_z in the equatorial plane of the magnetosphere at 1445 UT. The pink circle indicates the MMS 1 location. The DM results suggest that the observed electron and ion WSs took place just earthward of a global B_z-reversal region at about –30 R_E, consistent with the PIC simulation picture demonstrated by Sitnov et al. (2021b).

3.2.2. 3 July 2017 Event: Event 2

The second WS event, Event 2, took place at 0526:30–0527:15 UT on 3 July 2017 when the MMS tetrahedron was located at a downtail radial distance of ~18 R_E, (X, Y, Z) = (–17.6, 3.3, 1.7) R_E in GSM. The average interspacecraft separation was ~25 km during this interval. This event, close to a series of dipolarization fronts (DFs), was originally reported by Chen et al. (2019), who focused on the guide-field reconnection near EDRs. On the other hand, based on comparison with 3-D PIC simulations, Sitnov et al. (2021a) suggested that electron and ion WSs also manifested during this interval. Here we provide a more detailed analysis of the WS signatures using the MMS observations. Note that not all data from MMS 4

315 instruments are available for Event 2. Below we present field and plasma observations
316 obtained from MMS 1 in GSM coordinates, but these observations in an LMN coordinate
317 system and comparisons among all three probes are provided in Figures S5 and S6,
318 respectively.

319 Whereas Event 2 occurred under relatively quiet geomagnetic conditions just before a
320 small substorm initiated at ~0540 UT (Figure S4 in the SI), the DM-based reconstruction at
321 0525 UT (Figure 5) indicates that this WS event was located in a region of relatively small
322 B_z value earthward of a global X-line (B_z-reversal region) at the time of interest, similar to
323 the WS simulation picture (Sitnov et al., 2021a).

324 Figure 6 shows an overview of Event 2 observed by MMS 1 at 0526:30–0527:15 UT. It
325 is evident from Figure 6a that throughout this interval, the MMS 1 spacecraft encountered a
326 short-period flapping of the magnetotail current sheet characterized by strong B_x oscillations
327 with the amplitudes of ~10–20 nT and the periods of ~10–15 s. At ~0526:42 UT (marked by
328 gray shading), immediately before the first neutral sheet crossing (B_x = 0) due to the
329 magnetotail flapping, MMS 1 observed a transient, tailward-to-earthward electron flow
330 reversal in $V_{ex\perp}$ (i.e., electron WS) from approxymately –2,000 km s^{-1} to ~500–1,000 km s^{-1}
331 (Figure 6c). The electron WS, appearing in an earthward ion flow ($V_{ix\perp}$, Figure 6b), was not
332 accompanied by a sign reversal of B_z (Figure 6a). The B_z field and plasma density near the
333 electron WS were elevated from ~0 nT up to ~12 nT (Figure 6a) and from ~0.3 up to ~0.5
334 cm^{-3} (Figure 6d), respectively. Inside the electron WS region, the plasma β value (Figure 6e)
335 was greater than 10. According to Figure 6f, ions around the electron WS were

unmagnetized/agyrotropic, whereas electrons were magnetized.

Figure 7 presents a zoomed-in plot of the MMS 1 observations at 0526:40–0526:50 UT to characterize fields and plasma signatures in the vicinity of the electron WS. Such detailed field and plasma signatures confirm that the divergent electron flows at ~0526:42 UT occurred concurrently with positive B_z values (Figure 7a), earthward ion flows (Figure 7b), small dawnward bulk electron flow ($|V_{ey}| \leq 1{,}000$ km s^{-1}, Figure 6c), and small electric fields (particularly E_z in Figure 7f). Similar to Event 1, these features indicate that this electron WS occurred away from any electron-scale thin current sheet.

In the vicinity of this electron WS, one may notice that the energy conversion and the Joule heating rate had large values (up to 0.4 nW m^{-3}, Figure 7h) comparable to those in the T18 EDR, and that the parallel and perpendicular electron temperatures were locally enhanced (Figure 7g). The results suggest that this electron WS was a site of the significant energy conversion and electron heating. Moreover, the electron anisotropy had a stronger enhancement compared with Event 1.

Another interesting feature of Event 2 is that the electron WS had strong, localized negative and positive excursions in E_y ($|E_y| > 20$ mV m^{-1}, Figure 7f), corresponding to tailward and earthward electron convective motions in $V_{ex\perp}$. These motions are expected as a signature of the flux starvation effect associated with WSs in the wakes of DFs (Pritchett, 2015; Sitnov et al., 2021a).

3.2.3. 3 August 2020 Event: Event 3

The third WS event on 3 August 2020, Event 3, took place in an active magnetotail between two nearby substorm activations (Figure S7 in the SI). During Event 3, the MMS tetrahedron was located at ~28 R_E downtail, (X, Y, Z) = (–27.2, –5.1, 1.4) R_E in GSM. The separation of the MMS tetrahedron was ~35–40 km. The DM-based reconstruction at 0235 UT (Figure 8) indicates that Event 3 occurred in a region of small B_z value (~4 nT) earthward of a global X-line at the time of interest.

Figure 9 presents an overview of Event 3 observed by MMS 1 at 0234:15–0237:45 UT. As evident from Figures 9a and 9b, the interval started with a strong DF (B_z (or $|B|$) enhancement by ~18 nT) that occurred under fast earthward ion flow conditions with a speed of ~300 km s^{-1}. After the strong DF passed, MMS 1 encountered a minimum $|B|$ (~ 0 nT) at ~02:36:05 UT and then a small B_z enhancement with the amplitude < 10 nT. In the course of the small B_z enhancement, a transient electron flow reversal from apprpximately –1,000 to ~500 km s^{-1} emerged in the magnetotail CPS where N ~0.3 cm^{-3} (Figure 9d), $\beta > 10$ (Figure 9e), and $Q_i^{1/2}$ ~0.05 and $Q_e^{1/2}$ ~0.02 (Figure 9f). An interesting feature of this case is that under stable positive B_z (~5 nT) conditions after the electron WS at ~0236:13 UT, the ion velocity $V_{ix\perp}$ reversed its sign from positive to negative, which may be interpreted as a signature of ion WS. This reversal is also consistent with the WS simulation picture (Sitnov et al., 2021a).

We note that the strong variations of the B_z field seen in Figures 9a made applying the LMN coordinate system to Event 3 difficult. This is because the L component in LMN would be close to the x direction in GSM, as seen in earlier studies (Marshall et al., 2020). This

might suggest the filamentation of the original tail current sheet and even its strong bending, which would distort the global picture for this WS predicted by DM reconstruction (Figure 8). Thus, the subsequent analysis of Event 3 is limited to the GSM system.

Figure 10 shows a zoomed-in view of Event 3 for a 10-s interval of 0236:07.5–0236:17.5 UT with focus on the electron WS at ~0236:13 UT. It is clear that the electron WS properties share commonalities with those for Events 1 and 2: (1) weak duskward electron velocity enhancement, $|V_{ey}| < 1{,}000$ km s^{-1} (Figure 10c), compared with T18; (2) weak duskward current density, $|J_y| \leq 50$ nA m^{-2} (Figure 10e), compared with ~100 nA m^{-2} in T18; and (3) a small Hall electric field, $|E_z| < 5$ mV m^{-1} (Figure 10f), compared with ~30 mV m^{-1} in T18. Consistent with both Events 1 and 2, the energy conversion and Joule heating rate values are substantial up to ~0.2 nW m^{-3}. This result suggests that, similar to EDRs, the observed electron WS is a localized site of the strong energy conversion associated with either plasma instabilities and/or magnetic reconnection. We have also confirmed the consistency of these WS properties at all available MMS probes (Figure S8 in the SI).

3.2.4. Other Three Events: Events 4–6

Here we briefly describe other three WS events, Events 4–6, that took place at 1142:15–1143:15 UT and at 1148:15–1149:15 UT on 6 July 2018 and at 1756:30–1759:30 UT on 19 August 2018. During Events 4 and 5, the MMS spacecraft were located at (X, Y, Z) = (–13.2, 2.9, 3.6) R_E in GSM, whereas they were located at (X, Y, Z) = (–16.9, 3.2, 3.9) R_E in GSM during Event 6. Figure 11 presents the DM reconstructions and MMS 1 observations of

399 Events 4–6 (left, Event 4; center, Event 5; right, Figure 6). Further detailed descriptions and
400 data analyses for each event are provided in the SI.

401 In contrast to Events 1–3, where the WSs were located in regions of relatively small B_z
402 values in the stretched tail configuration and similar to the WS simulation picture by Sitnov
403 et al. (2021a), Events 4–6 were located in strongly dipolarized regions where B_z values
404 remained large (>15 nT, Figure 11b). The MMS observations are consistent with their global
405 DM reconstructions (Figures 11a), indicating that Events 4–6, being also located close to the
406 global X-lines, appeared in the regions/times of the magnetotail dipolarization. Events 4–6
407 exhibit rapid tailward-then-earthward motions of the dipolarized flux tubes with magnetized
408 electrons against the background of the earthward ion flows that changed to tailward flows
409 under large and positive B_z field conditions. Whereas these motions fit the formal definition
410 of plasma WSs, the mechanism for Events 4–6 is likely different from the pre-reconnection
411 processes described in Sitnov et al. (2021a), as will be discussed below.

412

413 ## 4. Summary and Discussion

414 In this study we have investigated the MMS observations of magnetotail plasma
415 divergent flows that change their direction from earthward to tailward or vice versa at radial
416 distances from –13 to –30 R_E. The key features of the observed electron and ion flow reversals
417 in the magnetotail can be summarized as follows:

418 1) Transient electron divergent flows of ~1,000–2,000 km s^{-1} in $V_{ex\perp}$ (electron WSs) are
419 embedded into a single, more gradually changing ion divergent flow in $V_{ix\perp}$ (ion WS).

In electron WSs, magnetized electrons are decoupled from demagnetized.

2) Electron WSs are not accompanied by concurrent sign changes of the northward magnetic field B_z (> 4 nT), in strong contrast with the T18 EDR. This indicates that the electron WSs are not associated with any rapid change in magnetic topology.

3) Electron WSs are not accompanied by any significant dawnward electron flows and the corresponding duskward current density enhancements, unlike the T18 EDR. In particular, the duskward electron flows are smaller than the divergent electron flows ($|V_{ey}| \leq |V_{ex}|$).

4) The Hall electric field, E_z, is rather weak inside the electron WS, compared with strong electric fields directed to the electron-scale and electron-dominated current sheet of the T18 EDR. The result indicates that electron WSs are formed away from EDRs.

5) The energy conversion and Joule heating rate in electron WSs are comparable with those in the EDR, although their specific distributions may differ. This is generally consistent with that fact that the relative difference between $|V_{ex\perp}|$ and $|(E\times B)_x/|B|^2|$ is significant in most (not all) of the presented electron WSs. Thus, it is suggested that that WSs are active regions of the energy exchange between the electromagnetic field and different plasma species and probably associated with the corresponding multiscale plasma instabilities and magnetic reconnection.

We confirmed for Events 1–6 that these conclusions are consistent for all available MMS probes. For Events 1 and 2 we also confirmed that the results in the original GSM coordinate

441 system are consistent with those in the LMN coordinate system. On the other hand,
442 applications of the GSM-to-LMN coordinate transformation to the other four events (Events
443 3–6) that were detected close to DFs or even just dominant B_z regions might be misleading
444 in the original context of the divergent tailward-to-earthward plasma flows because the
445 results would reflect the DF features. At the same time, the global context of the observed
446 WS events had been clarified by DM reconstruction of the global magnetospheric magnetic
447 field in the equatorial plane (Figures 4b, 5, 8, and 11a).

448 Our analysis shows that the observed divergent flows are drastically different from
449 reconnection outflows from EDRs. Instead, based on their distinctive features (key features
450 1–5 above), we interpret them as divergent plasma flows preceding the magnetic topology
451 change. The corresponding concept was originally introduced by Lin & Swift (2002) and
452 further developed by Siscoe et al. (2009) and Tanaka et al. (2019). Most recently, it was
453 elaborated as a multiscale and multispecies phenomenon by Sitnov et al. (2021a), who
454 reproduced electron and ion WSs using 3-D PIC simulations and introduced terms “plasma
455 watersheds” and “electron/ion watersheds” to distinguish those pre-reconnection phenomena
456 from more conventional reconnection outflows, as well as to separate WSs of different
457 plasma species.

458 In addition to the local MMS observations on electron scales, we have also provided a
459 global picture of the magnetotail reconnection by mining the historical space magnetometer
460 data (Stephens et al., 2019; Sitnov et al., 2019, 2021b). According to this picture, shown in
461 Figures 4b, 5, 8 and 11, the MMS spacecraft observing the ion and electron WSs were
462 consistently located just earthward of the global reconnection X-lines. Note here that the very

463 high fidelity of the X-line reconstruction using this DM method has recently been provided
464 by Stephens et al. (2022). This finding strongly suggests that all the observed WSs are indeed
465 associated with the magnetotail reconnection processes. It also suggests the possibility that
466 the WSs preceded the subsequent or secondary reconnection processes earthward of the
467 global X-lines.

468 Because the reported electron WSs do not coincide with similar ion WSs and occur in
469 earthward and rather weakly disturbed convective ion flows, one may attempt to interpret the
470 $V_{ex\perp}$ reversal jets in terms of electron-only reconnection regimes, similar to those observed
471 by MMS in the turbulent magnetosheath (Phan et al., 2018). Indeed, the electron-only
472 reconnection is maintained by super-Alfvénic electron flow reversals accompanied by the
473 reversals of the magnetic field normal to the current sheet plane in the absence of the
474 corresponding ion outflows. However, the electron WSs are not accompanied by any normal
475 magnetic field reversals. Furthermore, the electron WSs are often embedded in a larger-scale
476 ion WS, whereas the electron-only reconnection is not accompanied by any ion reversal jets.
477 Thus, the observed electron WSs cannot be explained in terms of the electron-only
478 reconnection.

479 At the same time, the formation of WSs as a result of the ion tearing instability and/or
480 the subsequent DF dynamics suggested by 3-D PIC simulations (Sitnov et al., 2021b) is not
481 the only possible WS-formation mechanism. Another possible mechanism is kinetic
482 ballooning/interchange instability (BICI), which can also provide plasma divergent flows
483 (Panov et al., 2012a). Indeed, if the instability region passes transversely across the spacecraft
484 in the y direction, it might observe similar $V_{ex\perp}$ reversals due to the azimuthal structure of the

485 instability (Figure 11 in Panov et al., 2012a). The BICI interpretation may be particularly
486 relevant to Events 4–6 because they occurred in strongly dipolarized regions with large B_z
487 values. However, there are also important distinctions between WSs and conventional BICI
488 perturbations. First, the fast flows in BICI are often field-aligned (Panov et al., 2012b;
489 Pritchett et al., 2014). Second, in both simulations (Pritchett and Coroniti, 2010) and
490 observations (Panov et al., 2012a, 2012b), BICI-related divergent flows appear as a sawtooth-
491 like structure, whereas WSs exhibit solitary perturbations with comparable field-aligned and
492 perpendicular flows or with dominant perpendicular flows. Third, in BICI, the electron
493 velocity oscillations are accompanied by similar B_x and B_z perturbations (e.g., Figure 10 in
494 Panov et al., 2012a) even if they do not change the magnetic topology.

495 On the other hand, the onset of reconnection caused by BICI waves discovered in some
496 BICI simulations (Pritchett and Coroniti, 2013) and observations (Panov et al., 2020) may
497 resemble the WS onset mechanism (Sitnov et al., 2021a) with the main difference being that
498 the specific non-reconnection instability generates the divergent plasma motions that cause
499 the topology change. In the case of BICI, these are buoyant motions of plasma with different
500 electron and ion motions due to the lower-hybrid drift effects (Huba et al., 1977). In the case
501 of WS, this is the ion-tearing instability (Schindler, 1974; Sitnov and Schindler, 2010; Sitnov
502 et al., 2013, 2021a; Bessho and Bhattacharjee, 2014; Pritchett, 2015), which involves
503 different motions of unmagnetized ions and magnetized electrons. Further separation of these
504 mechanisms requires comprehensive multiprobe investigations with the probe arrays
505 extended both along and across the tail current sheet (e.g., Kepko, 2018).

506 The WS regime belongs to a broader class of flow-driven reconnection processes, such

507 as the magnetic shear instability in accretion disks (Hawley and Balbus, 1992), kink
508 instability of the flux ropes in the solar corona (Török and Kliem, 2005; Markidis et al., 2014),
509 reconnection driven by the electron dynamics in laser-produced plasma (Kuramitsu et al.,
510 2018) and by the Kelvin-Helmholtz instability at the magnetopause (Ma et al., 2014;
511 Nakamura et al., 2017), and the shock-driven reconnection (Bessho et al., 2022), which is
512 gaining more and more attention in reconnection physics (Ji et al., 2022). The special place
513 occupied by WS in this class is explained by the fact that WSs are driven by a natural
514 reconnection-like (tearing) instability, which is driven by the mutual attraction of the parallel
515 current filaments. The non-reconnection regime is explained by the initial magnetization of
516 electrons (so that the dissipation is provided by the Landau resonance with unmagnetized
517 ions (Schindler, 1974)) and the development of DFs in its nonlinear phase (e.g., Sitnov and
518 Swisdak, 2011; Sitnov et al., 2013). Indeed, Events 2–6 developed in the DF trailing region.

519 To conclude, the concept of plasma WSs, introduced two decades ago (Lin and Swift,
520 2002) and recently reiterated on the fully kinetic level in 3-D PIC simulations (Sitnov et al.,
521 2021a), offers an interesting alternative to the paradigm of divergent flows as a consequence
522 of the magnetic topology change. In this study, using the high-resolution MMS measurements,
523 we have provided the characteristic fields and plasma variations of electron and ion WSs.
524 The features we describe share many similarities with those predicted in simulations and help

525 separate WSs from processes near the EDR and electron-only reconnection regimes.

526

527

528 **Acknowledgements.**

529 This work was supported by NASA grants (80NSSC19K0847 and 80NSSC20K0699). We
530 are grateful to the entire MMS team for providing high-resolution fields and plasma data for
531 this study. Specifically, we thank J. L. Burch, MMS principal investigator, and the following
532 instrument lead co-investigators: R. B. Torbert for FIELDS, C. T. Russell for FGM, R. E.
533 Ergun and P.-A. Lindqvist for EDP, and C. Pollock and B. L. Giles for FPI.

534

535 **Data Availability Statement**

536 The MMS data used in this study are publicly available at
537 https://lasp.colorado.edu/mms/sdc/public/. The SMU and SML indices are available on the
538 SuperMAG website (https://supermag.jhuapl.edu/). SuperMAG is an international
539 collaboration with many organizations and institutes, and it is funded by National Science
540 Foundation. The OMNI solar wind data are publicly available at
541 https://omniweb.gsfc.nasa.gov. DM results are available at
542 https://doi.org/10.5281/zenodo.6401960.

References

Angelopoulos, V., Artemyev, A., Phan, T.D. et al. (2020), Near-Earth magnetotail reconnection powers space storms. Nat. Phys. 16, 317–321, https://doi.org/10.1038/s41567-019-0749-4

Baker, D. N., Pulkkinen, T. I., Angelopoulos, V., Baumjohann, W., and McPherron, R. L. (1996), Neutral line model of substorms: Past results and present view, J. Geophys. Res., 101(A6), 12975– 13010, doi:10.1029/95JA03753.

Bandyopadhyay, R., Chasapis, A., Matthaeus, W. H., Parashar, T. N., Haggerty, C. C., Shay, M. A., Gershman, D. J., Giles, B. L., and Burch, J. L. (2021), Energy dissipation in turbulent reconnection, Physics of Plasmas 28, 112305 https://doi.org/10.1063/5.0071015

Baumjohann, W., Paschmann, G., and Cattell, C. A. (1989), Average plasma properties in the central plasma sheet, J. Geophys. Res., 94(A6), 6597–6606, doi:10.1029/JA094iA06p06597.

Bessho, N, and A. Bhattacharjee (2014), Instability of the current sheet in the Earth's magnetotail with normal magnetic field. Phys. Plasmas 21(1), 102905

Bessho, N., Chen, L. J., Stawarz, J. E. , Wang, S. , Hesse, M., Wilson, L. B. , Ng, J. (2022) Strong reconnection electric fields in shock-driven turbulence, Phys. Plasmas 29, 042304. https://doi.org/10.1063/5.0077529

Birn, J., & Hesse, M. (2005). Energy release and conversion by reconnection in the magnetotail. Annales Geophysicae, 23(10), 3365–3373. https://doi.org/10.5194/angeo-23-3365-2005

Burch, J. L., et al. (2016), Magnetospheric Multiscale overview and science objectives, Space Sci. Rev., 199, 5 – 21, doi: 10.1007/s11214-015-0164-9

Chen, L. J., Wang, S., Hesse, M., Ergun, R. E., Moore, T., Giles, B., et al. (2019). Electron diffusion regions in magnetotail reconnection under varying guide fields. Geophysical Research

Letters, 46(12), 6230–6238. https://doi.org/10.1029/2019GL082393

Dungey, J. W. (1961). Interplanetary magnetic field and the Auroral Zones. Physical Review Letters, 6, 47–48. https://doi.org/10.1103/PhysRevLett.6.47

Eastwood, J. P., Phan, T. D., Øieroset, M., and Shay, M. A. (2010a), Average properties of the magnetic reconnection ion diffusion region in the Earth's magnetotail: The 2001–2005 Cluster observations and comparison with simulations, J. Geophys. Res., 115, A08215, doi:10.1029/2009JA014962.

Eastwood, J. P., Shay, M. A., Phan, T. D., & Øieroset, M. (2010b). Asymmetry of the ion diffusion region Hall electric and magnetic fields during guide field reconnection: Observations and comparison with simulations. Physical Review Letters, 104(20), 205001. https://doi.org/10.1103/PhysRevLett.104.205001

Eastwood, J. P., Sibeck, D. G., Slavin, J. A., Goldstein, M. L., Lavraud, B., Sitnov, M., Imber, S., Balogh, A., Lucek, E. A., and Dandouras, I. (2005), Observations of multiple X-line structure in the Earth's magnetotail current sheet: A Cluster case study, Geophys. Res. Lett., 32, L11105, doi:10.1029/2005GL022509

Ergun, R.E., Tucker, S., Westfall, J. et al. (2016), The Axial Double Probe and Fields Signal Processing for the MMS Mission. Space Sci Rev 199, 167–188, https://doi.org/10.1007/s11214-014-0115-x

Farrugia, C. J., Rogers, A. J., Torbert, R. B., Genestreti, K. J., Nakamura, T. K. M., Lavraud, B., et al. (2021). An encounter with the ion and electron diffusion regions at a flapping and twisted tail current sheet. Journal of Geophysical Research: Space Physics, 126, e2020JA028903. https://doi.org/10.1029/2020JA028903

Genestreti, K. J., Nakamura, T. K. M., Nakamura, R., Denton, R. E., Torbert, R. B., Burch, J. L., et al. (2018). How accurately can we measure the reconnection rate EM for the MMS

591 diffusion region event of 11 July 2017?, Journal of Geophysical Research: Space Physics,
592 123, 9130– 9149. https://doi.org/10.1029/2018JA025711
593 Hawley, J. F., and S. A. Balbus (1992), A Powerful Local Shear Instability in Weakly Magnetized
594 Disks. III. Long-Term Evolution in a Shearing Sheet, Astrophysical Journal v.400, p.595
595 Hones, E.W., Jr. (1984). Plasma Sheet Behavior During Substorms. In Magnetic Reconnection in
596 Space and Laboratory Plasmas, E.W. Hones (Ed.). https://doi.org/10.1029/GM030p0178
597 Huba, J.D., Gladd, N.T. and Papadopoulos, K. (1977), The lower-hybrid-drift instability as a
598 source of anomalous resistivity for magnetic field line reconnection. Geophys. Res. Lett.,
599 4: 125-128. https://doi.org/10.1029/GL004i003p00125
600 Ji, H., Daughton, W., Jara-Almonte, J. et al. (2022), Magnetic reconnection in the era of exascale
601 computing and multiscale experiments. Nat Rev Phys. https://doi.org/10.1038/s42254-
602 021-00419-x
603 Kepko L. (2018), Magnetospheric Constellation: Leveraging Space 2.0 for Big Science, IEEE,
604 18244840, DOI: 10.1109/IGARSS.2018.8519475
605 Kuramitsu, Y., Moritaka, T., Sakawa, Y. et al. (2018) Magnetic reconnection driven by electron
606 dynamics. Nat Commun 9, 5109. https://doi.org/10.1038/s41467-018-07415-3
607 Lin, Y., & Swift, D. W. (2002). Generation of near-earth reconnection by divergent flows in the
608 plasma sheet. Journal of Geophysical Research, 107(A11), SMP1–SMP9.
609 https://doi.org/10.1029/2002JA009308
610 Lindqvist, PA., Olsson, G., Torbert, R.B. et al. (2016), The Spin-Plane Double Probe Electric Field
611 Instrument for MMS. Space Sci Rev 199, 137–165, https://doi.org/10.1007/s11214-014-
612 0116-9
613 Liu, Y.-H., Birn, J., Daughton, W., Hesse, M., and Schindler, K. (2014), Onset of reconnection in
614 the near magnetotail: PIC simulations, J. Geophys. Res. Space Physics, 119, 9773– 9789,

615 doi:10.1002/2014JA020492.
616 Markidis, S., Lapenta, G., Delzanno, G. L., Henri, P., Goldman, M. V., Newman, D. L., Intrator,
617 T., Laure, E. (2014), Signatures of secondary collisionless magnetic reconnection driven
618 by kink instability of a flux rope, Plasma Physics and Controlled Fusion, 064010,
619 doi:10.1088/0741-3335/56/6/064010 56,
620 Marshall, A. T., Burch, J. L., Reiff, P. H., Webster, J. M., Torbert, R. B., Ergun, R. E., et al. (2020).
621 Asymmetric reconnection within a flux rope-type dipolarization front. Journal of
622 Geophysical Research: Space Physics, 125, e2019JA027296.
623 https://doi.org/10.1029/2019JA027296
624 Ma, X., Otto, A., & Delamere, P. A. (2014). Interaction of Magnetic Reconnection and Kelvin-
625 Helmholtz Modes for Large Magnetic Shear: 2. Reconnection Trigger. Journal of
626 Geophysical Research: Space Physics, 119(2). https://doi.org/10.1002/2013JA019225
627 Nagai, T., Shinohara, I., Fujimoto, M., Matsuoka, A., Saito, Y., and Mukai, T. (2011), Construction
628 of magnetic reconnection in the near-Earth magnetotail with Geotail, J. Geophys. Res.,
629 116, A04222, doi:10.1029/2010JA016283.
630 Nakamura, T. K. M., Hasegawa, H., Daughton, W., Eriksson, S., Li, W. Y., & Nakamura, R. (2017).
631 Turbulent mass transfer caused by vortex induced reconnection in collisionless
632 magnetospheric plasmas. Nature Communications, 8, 1582.
633 https://doi.org/10.1038/s41467-017-01579-0
634 Øieroset, M., T. D. Phan, M. Fujimoto, R. P. Lin, and R. P. Lepping (2001), In situ detection of
635 collisionless reconnection in the Earth's magnetotail, Nature, 412, 414.
636 Panov, E. V., et al. (2012a), Kinetic ballooning/interchange instability in a bent plasma sheet, J.
637 Geophys. Res., 117, A06228, doi:10.1029/2011JA017496.
638 Panov, E. V., Sergeev, V. A., Pritchett, P. L., Coroniti, F. V., Nakamura, R., Baumjohann, W.,

Angelopoulos, V., Auster, H. U., and McFadden, J. P. (2012b), Observations of kinetic ballooning/interchange instability signatures in the magnetotail, Geophys. Res. Lett., 39, L08110, doi:10.1029/2012GL051668.

Panov, E. V., Lu, S., & Pritchett, P. L. (2020). Understanding spacecraft trajectories through detached magnetotail interchange heads. Journal of Geophysical Research: Space Physics, 125, e2020JA027930. https://doi.org/10.1029/2020JA027930

Phan, T. D., Eastwood, J. P., Shay, M. A., Drake, J. F., Sonnerup, B. U. Ö., Fujimoto, M., et al. (2018). Electron magnetic reconnection without ion coupling in Earth's turbulent magnetosheath. Nature, 557(7704), 202–206. https://doi.org/10.1038/s41586-018-0091-5

Pollock, C., Moore, T., Jacques, A. et al. (2016), Fast Plasma Investigation for Magnetospheric Multiscale. Space Sci Rev 199, 331–406, https://doi.org/10.1007/s11214-016-0245-4

Pritchett, P. L., and F. V.Coroniti (2010), A kinetic ballooning/interchange instability in the magnetotail, J. Geophys. Res., 115, A06301, doi:10.1029/2009JA014752.

Pritchett, P. L., and Coroniti, F. V. (2013), Structure and consequences of the kinetic ballooning/interchange instability in the magnetotail, J. Geophys. Res. Space Physics, 118, 146– 159, doi:10.1029/2012JA018143.

Pritchett, P. L., Coroniti, F. V., and Nishimura, Y. (2014), The kinetic ballooning/interchange instability as a source of dipolarization fronts and auroral streamers, J. Geophys. Res. Space Physics, 119, 4723– 4739, doi:10.1002/2014JA019890.

Pritchett, P.L. (2015), Instability of current sheets with a localized accumulation of magnetic flux. Phys. Plasmas 22(6), 062102

Rogers, A. J., Farrugia, C. J., & Torbert, R. B. (2019). Numerical algorithm for detecting ion diffusion regions in the geomagnetic tail with applications to MMS tail season 1 May to

30 September 2017. Journal of Geophysical Research: Space Physics, 124, 6487– 6503. https://doi.org/10.1029/2018JA026429

Runov, A., et al. (2003), Current sheet structure near magnetic X-line observed by Cluster, Geophys. Res. Lett., 30, 1579, doi:10.1029/2002GL016730, 11.

Russell, C.T., Anderson, B.J., Baumjohann, W. et al. (2016), The Magnetospheric Multiscale Magnetometers. Space Sci Rev 199, 189–256, https://doi.org/10.1007/s11214-014-0057-3

Schindler, K. (1974), A theory of the substorm mechanism, J. Geophys. Res., 79(19), 2803–2810, doi:10.1029/JA079i019p02803.

Siscoe, G. L., Kuznetsova, M. M., & Raeder, J. (2009). Search for an onset mechanism that operates for both CMEs and substorms. Annales Geophysicae, 27(8), 3141–3146. https://doi.org/10.5194/angeo-27-3141-2009

Sitnov, M. I., and K. Schindler (2010), Tearing stability of a multiscale magnetotail current sheet, Geophys. Res. Lett., 37, L08102, doi:10.1029/2010GL042961.

Sitnov, M. I., and Swisdak, M. (2011), Onset of collisionless magnetic reconnection in two-dimensional current sheets and formation of dipolarization fronts, J. Geophys. Res., 116, A12216, doi:10.1029/2011JA016920.

Sitnov, M. I., N. Buzulukova, M. Swisdak, V. G. Merkin, and T. E. Moore (2013), Spontaneous formation of dipolarization fronts and reconnection onset in the magnetotail, Geophys. Res. Lett., 40(1), 22– 27, doi:10.1029/2012GL054701

Sitnov, M. I., Merkin, V. G., Roytershteyn, V., & Swisdak, M. (2018). Kinetic dissipation around a dipolarization front. Geophysical Research Letters, 45, 4639– 4647. https://doi.org/10.1029/2018GL077874

Sitnov, M. I., Stephens, G. K., Tsyganenko, N. A., Miyashita, Y., Merkin, V. G., Motoba, T., et al.

(2019). Signatures of nonideal plasma evolution during substorms obtained by mining multimission magnetometer data. Journal of Geophysical Research: Space Physics, 124(11), 8427–8456. https://doi.org/10.1029/2019JA027037

Sitnov, M. I., Motoba, T., & Swisdak, M. (2021a). Multiscale nature of the magnetotail reconnection onset. Geophysical Research Letters, 48, e2021GL093065. https://doi.org/10.1029/2021GL093065

Sitnov, M. I., Stephens, G., Motoba, T., & Swisdak, M. (2021b). Data mining reconstruction of magnetotail reconnection and implications for its first-principle modeling. Frontiers in Physiology, 9. https://doi.org/10.3389/fphy.2021.644884

Stephens, G. K., Sitnov, M. I., Korth, H., Tsyganenko, N. A., Ohtani, S., Gkioulidou, M., & Ukhorskiy, A. Y. (2019). Global empirical picture of magnetospheric substorms inferred from multimission magnetometer data. Journal of Geophysical Research: Space Physics, 124(0), 1085–1110. https://doi.org/10.1029/2018JA025843

Stephens, G. K., Sitnov, M. I., Weigel, R. S., Turner, D. L., Tsyganenko, N. A., Rogers, A. J., Genestreti, K. J., & Slavin J. A. (2022). Global structure of magnetotail reconnection revealed by mining space magnetometer data [Preprint]. Earth and Space Science Open Archive. https://doi.org/10.1002/essoar.10511996.1

Swisdak, M. (2016), Quantifying gyrotropy in magnetic reconnection, Geophys. Res. Lett., 43, 43– 49, doi:10.1002/2015GL066980.

Tanaka, T., Ebihara, Y., Watanabe, M., Den, M., Fujita, S., Kikuchi, T., et al. (2019). Development of magnetic topology during the growth phase of the substorm inducing the onset of the near-Earth neutral line. Journal of Geophysical Research: Space Physics, 124(7), 5158–5183. https://doi.org/10.1029/2018JA026386

Torbert, R.B., Russell, C.T., Magnes, W. et al. (2016), The FIELDS Instrument Suite on MMS:

711 Scientific Objectives, Measurements, and Data Products. Space Sci Rev 199, 105–135,
712 https://doi.org/10.1007/s11214-014-0109-8
713 Torbert, R. B., J. L. Burch, T. D. Phan, M. Hesse, M. R. Argall, J. Shuster, et al. (2018), Electron-
714 scale dynamics of the diffusion region during symmetric magnetic reconnection in space,
715 Science, 362 (6421), 1391 – 1395, doi: 10.1126/science.aat2998.
716 Török, T. and B. Kliem (2005), Confined and Ejective Eruptions of Kink-unstable Flux Ropes,
717 The Astrophysical Journal, Vol 630, L97
718 Yang, Y., Matthaeus, W. H., Parashar, T. N., Haggerty, C. C., Roytershteyn, V., Daughton, W., et
719 al. (2017). Energy transfer, pressure tensor, and heating of kinetic plasma. Physics of
720 Plasmas, 24(7), 072306. https://doi.org/10.1063/1.4990421
721 Zenitani, S., Hesse, M., Klimas, A., & Kuznetsova, M. (2011). New measure of the dissipation
722 region in collisionless magnetic reconnection. Physical Review Letters, 106, 195003-1–
723 195003-4. https://doi.org/10.1103/PhysRevLett.106.195003

Figure Captions

Figure 1. Summary plots of MMS 3 observations of the EDR event at 2233:45–2234:15 UT on 11 July 2017. (a) Three components and the strength of the magnetic field in GSM coordinates (B_x, blue; B_y, green; B_z, red; and $|B|$, black). (b) x component of the perpendicular ion velocity ($V_{ix\perp}$) in GSM coordinates. (c) x component of the perpendicular electron velocity ($V_{ex\perp}$, black) and $(\mathbf{E}\times\mathbf{B})_x/|B|^2$ (blue) in GSM coordinates. (d) N_e (red) and N_i (black). (e) Plasma β. and (f) Agyrotropy parameter, $Q^{1/2}$; $Q_e^{1/2}$ for electrons (red) and $Q_i^{1/2}$ for ions (black). Vertical dashed line and gray shading denote the reversal time (t_r) of $V_{ex\perp}$ at 2234:03 UT and a $t_r \pm 1$ s range, respectively.

Figure 2. Same format as Figure 1, but for MMS 1 observations of Event 1 at 1446:00–1448:30 UT on 2 August 2020. Gray shading denotes the electron WS.

Figure 3. Zoomed-in plots of Event 1 for a 10-s interval of 1446:30–1446:40 UT on 2 August 2020, which appears between dashed lines in Figure 2. (a) Magnetic field in GSM coordinates (B_x, blue; B_y, green; B_z, red; and $|B|$, black). (b) Ion velocity in GSM coordinates (V_{ix}, blue; V_{iy}, green; and V_{iz}, red). (c) Electron velocity in GSM coordinates (V_{ex}, blue; V_{ey}, green; and V_{ez}, red). (d) $V_{ex\perp}$ (red), $V_{ix\perp}$ (black), and $(\mathbf{E}\times\mathbf{B})_x/|B|^2$ (blue) in GSM coordinates. (e) Current density in GSM coordinates (J_x, blue; J_y, green; J_z, red; and $J_{\|}$, black). (f) Electric field in GSM coordinates (E_x, blue; E_y, green; E_z, red; and $E_{\|}$, black). (g) $T_{e\perp}$ (red) and $T_{e\|}$ (black). (h) $\boldsymbol{J}\cdot\boldsymbol{E}$ (black) and $\boldsymbol{J}\cdot\boldsymbol{E_e'}$ (red). (i) Ion and electron agyrotropies, $Q_i^{1/2}$ (black) and $Q_e^{1/2}$ (red). Dashed line and gray shading denote the reversal time (t_r = ~1446:36.1 UT) of $V_{ex\perp}$ and a $t_r \pm 1$ s range, respectively.

Figure 4. Data mining (DM) reconstructions of the magnetic field during Event 1 on 2 August 2020 (day of year: 215). (a) Comparison between the DM-reconstructed and observed magnetic field at MMS 1 for the interval of 1100–1500 UT. Dashed line is drawn at 1445 UT when MMS 1 was closest to the WS. (b) A snapshot of B_z distribution in the equatorial plane at 1445 UT. Pink circle denotes the MMS 1 location.

Figure 5. Same as Figure 4b but for Event 2 at 0525 UT on 3 July 2017 (day of year: 184). Pink circle denotes the MMS location.

Figure 6. Same format as Figure 1, but for MMS 1 observations of Event 2 at 0526:30–0527:15 UT on 3 July 2017. Gray shading denotes the electron WS.

Figure 7. Same format as Figure 3, but for Event 2 at 0526:40–0526:50 UT on 3 July 2017, which appears between dashed lines in Figure 6. Dashed line and gray shading denote the reversal time (t_r = ~0526:42.7 UT) of $V_{ex\perp}$ and a $t_r \pm 1$ s range, respectively.

Figure 8. Same as Figure 4b but for Event 3 at 0235 UT on 3 August 2020 (day of year: 216). Pink circle denotes the MMS location.

Figure 9. Same format as Figure 1, but for MMS 1 observations of Event 3 at 0234:15–0237:45 UT on 3 August 2020. Gray shading denotes the electron WS.

Figure 10. Same format as Figure 3, but for Event 3 at 0236:07.5–0236:17.5 UT on 3 August 2020, which appears between dashed lines in Figure 9. Dashed line and gray shading denote the reversal time (t_r = ~0236:12.9 UT) of $V_{ex\perp}$ and a $t_r \pm 1$ s range, respectively.

Figure 11. DM reconstructions and MMS 1 observations of other three WS events: Event 4 (left) and Event 5 (center) on 6 July 2018 and Event 6 (right) on 19 August 2018. (a) Same format as Figure 4b but for Event 4 (1140 UT), Event 5 (11:50 UT), and Event 6 (1755 UT). (b-g) Same format as Figures 1a-1f but for Events 4–6. Gray shadings denote the electron WSs.

Figure 1.

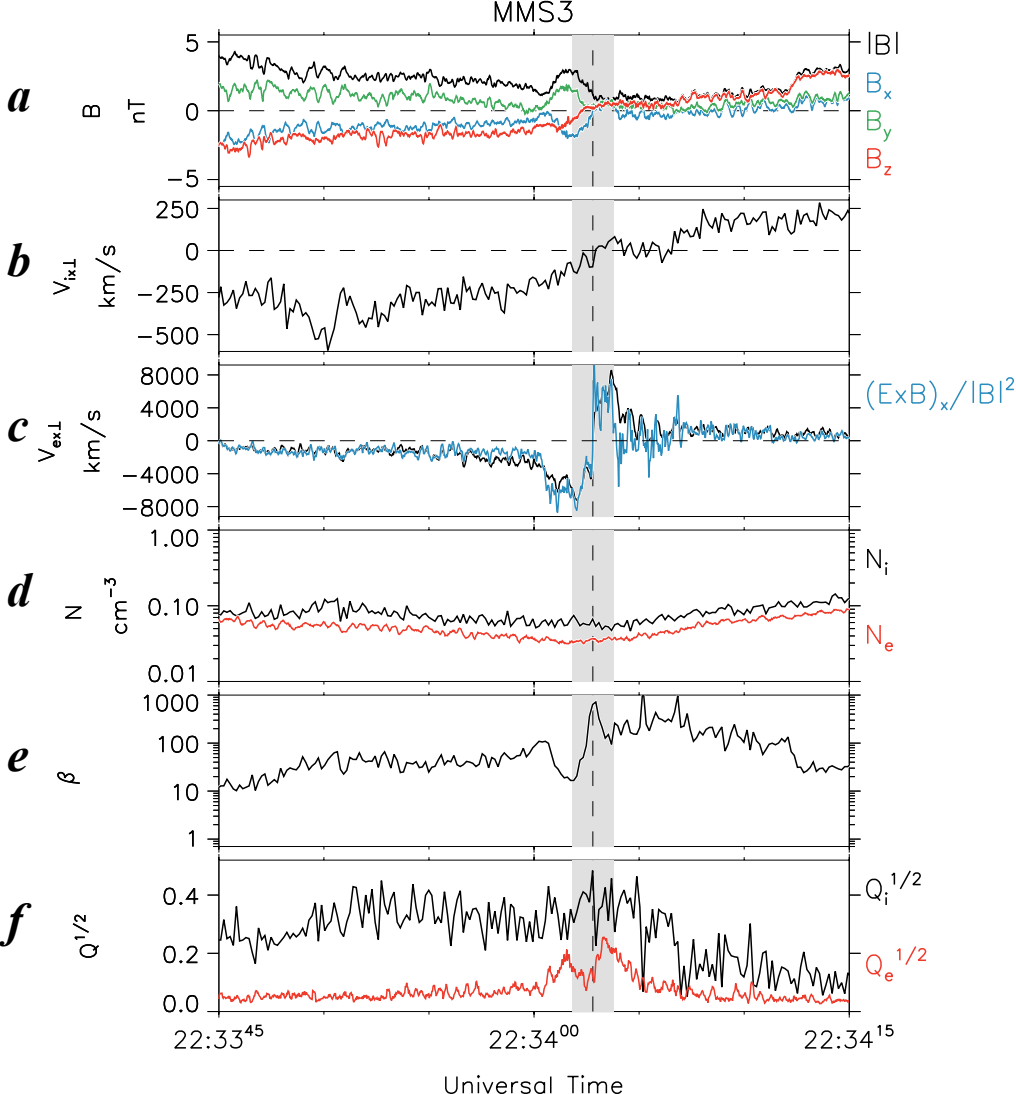
MMS3
a
B
nT
5
0
−5
|B|
B_x
B_y
B_z
b
$V_{ix\perp}$
km/s
250
0
−250
−500
c
$V_{ex\perp}$
km/s
8000
4000
0
−4000
−8000
$(ExB)_x/|B|^2$
d
N
cm^{-3}
1.00
0.10
0.01
N_i
N_e
e
β
1000
100
10
1
f
$Q^{1/2}$
0.4
0.2
0.0
$Q_i^{1/2}$
$Q_e^{1/2}$
22:33[45]
22:34[00]
22:34[15]
Universal Time

Figure 2.

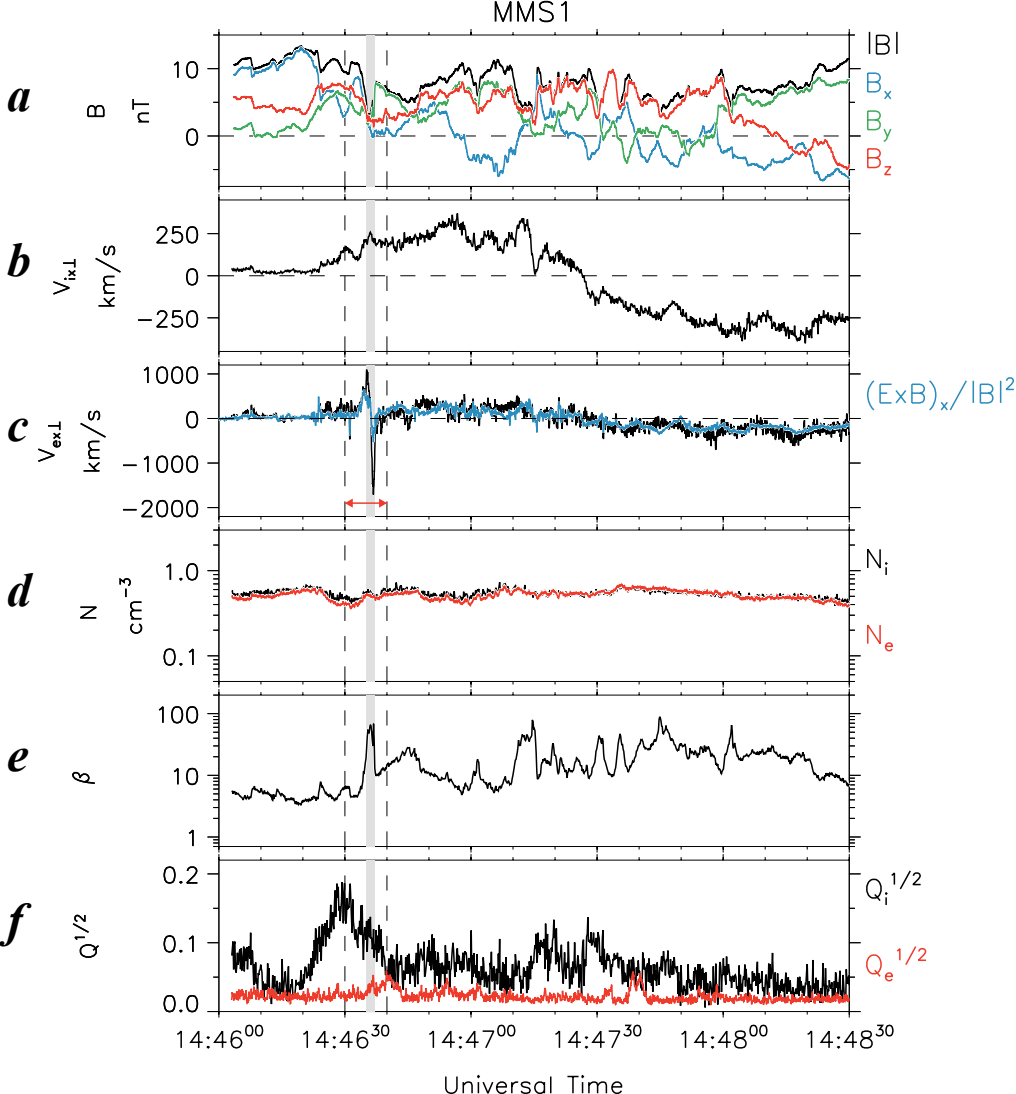
MMS1
a
B
nT
10
0
|B|
B_x
B_y
B_z
b
$V_{ix\perp}$
km/s
250
0
−250
c
$V_{ex\perp}$
km/s
1000
0
−1000
−2000
$(ExB)_x/|B|^2$
d
N
cm^{-3}
1.0
0.1
N_i
N_e
e
β
100
10
1
f
$Q^{1/2}$
0.2
0.1
0.0
$Q_i^{1/2}$
$Q_e^{1/2}$
14:46^{00}
14:46^{30}
14:47^{00}
14:47^{30}
14:48^{00}
14:48^{30}
Universal Time

Figure 3.

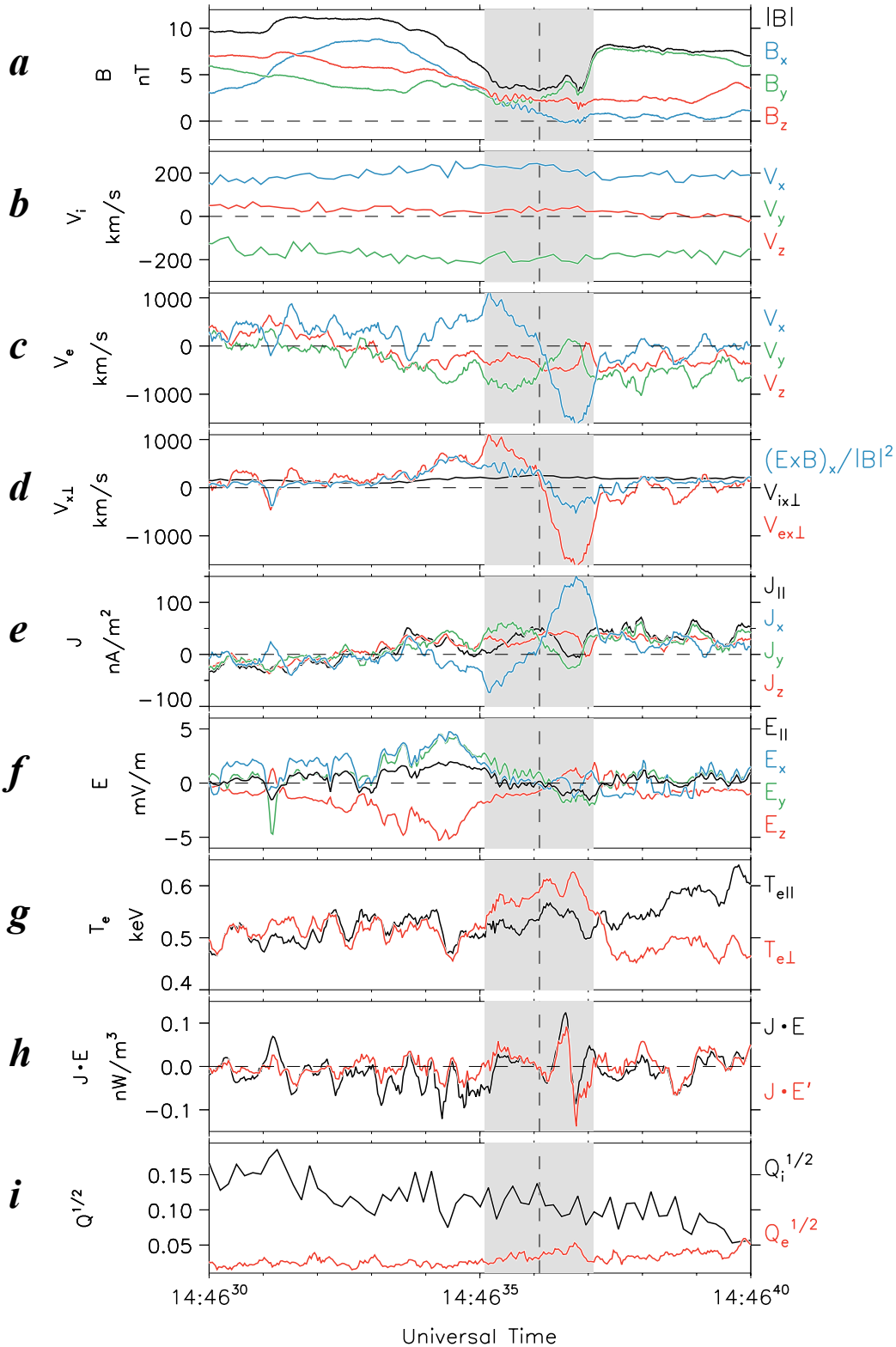
a
B
nT
10
5
0
|B|
B_x
B_y
B_z
b
V_i
km/s
200
0
−200
V_x
V_y
V_z
c
V_e
km/s
1000
0
−1000
V_x
V_y
V_z
d
$V_{x\perp}$
km/s
1000
0
−1000
$(ExB)_x/|B|^2$
$V_{ix\perp}$
$V_{ex\perp}$
e
J
nA/m^2
100
0
−100
$J_{||}$
J_x
J_y
J_z
f
E
mV/m
5
0
−5
$E_{||}$
E_x
E_y
E_z
g
T_e
keV
0.6
0.5
0.4
$T_{e||}$
$T_{e\perp}$
h
J•E
nW/m^3
0.1
0.0
−0.1
J•E
J•E′
i
$Q^{1/2}$
0.15
0.10
0.05
$Q_i^{1/2}$
$Q_e^{1/2}$
14:46^{30}
14:46^{35}
14:46^{40}
Universal Time

Figure 4.

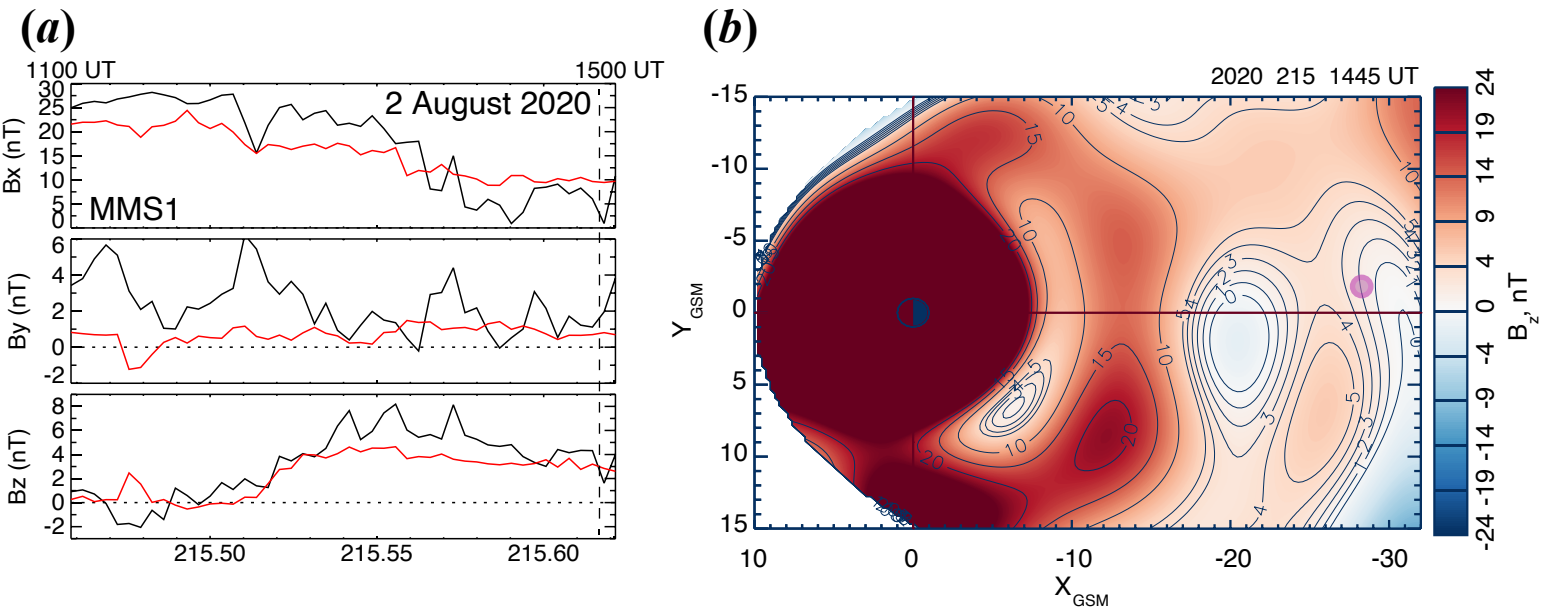
(a)
1100 UT
1500 UT
2 August 2020
MMS1
Bx (nT)
By (nT)
Bz (nT)
215.50
215.55
215.60
(b)
2020 215 1445 UT
Y GSM
X GSM
B z, nT

Figure 5.

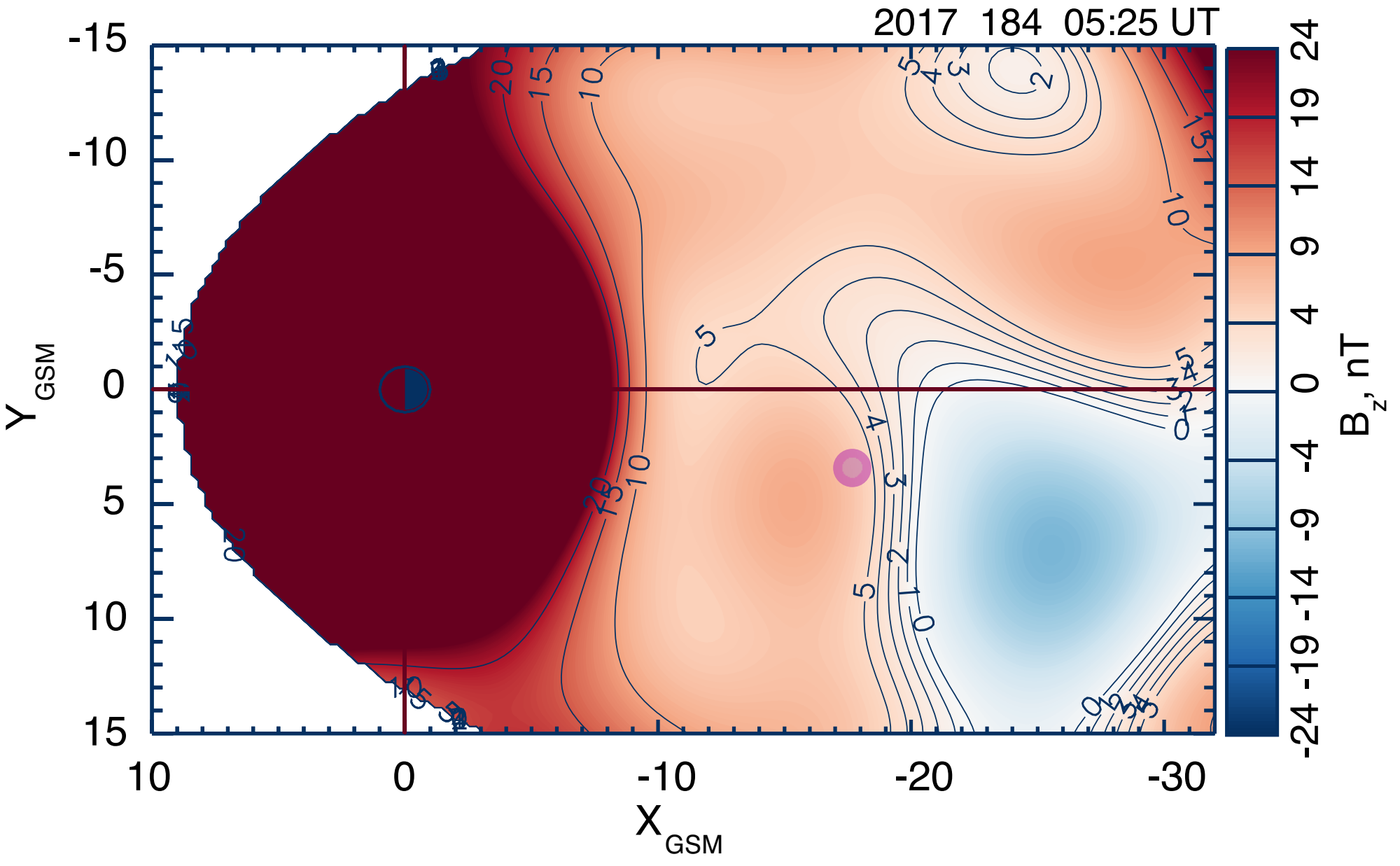
2017 184 05:25 UT
Y GSM
X GSM
B z, nT
-15
-10
-5
0
5
10
15
10
0
-10
-20
-30
24
19
14
9
4
0
-4
-9
-14
-19
-24

Figure 6.

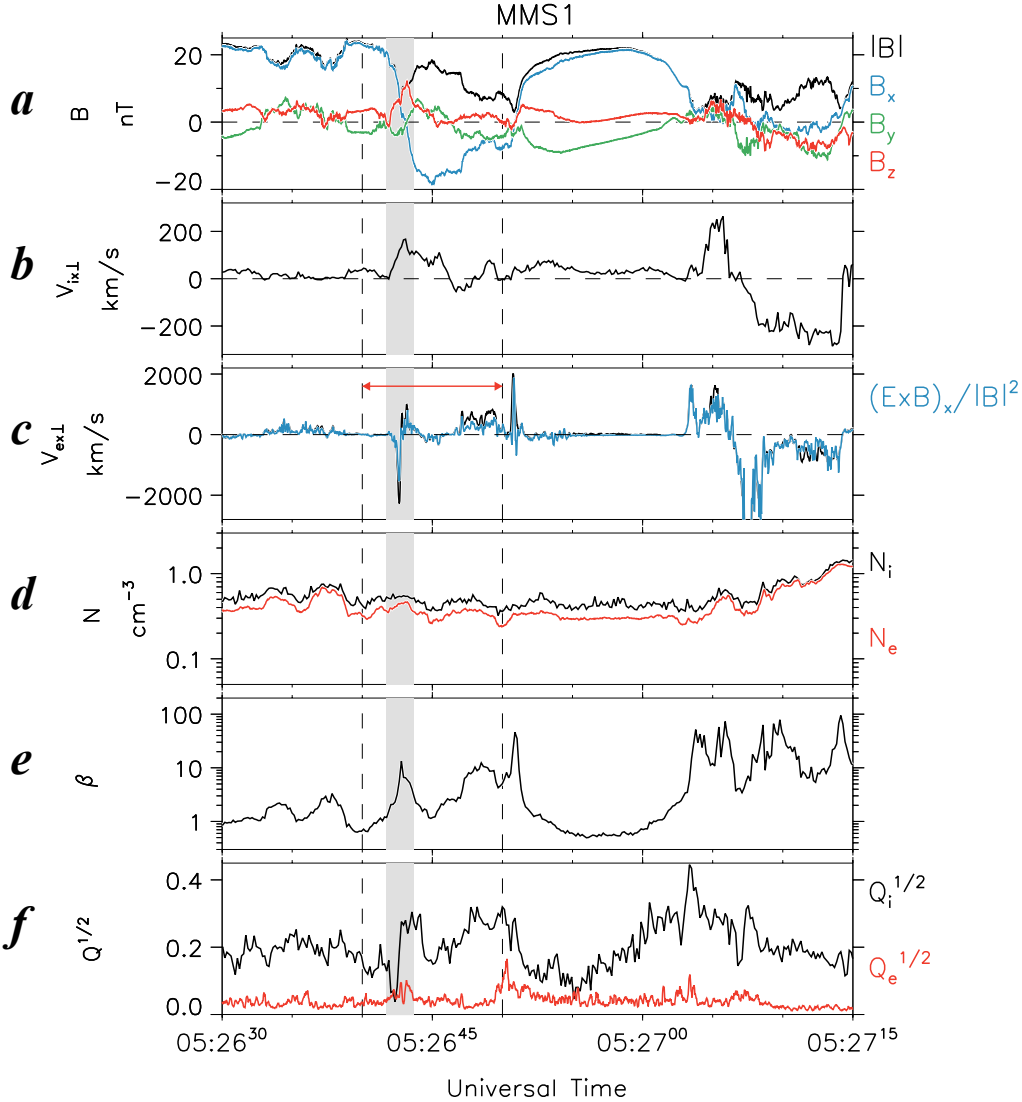
MMS1
a
B
nT
20
0
−20
|B|
B_x
B_y
B_z
b
$V_{ix\perp}$
km/s
200
0
−200
c
$V_{ex\perp}$
km/s
2000
0
−2000
$(ExB)_x/|B|^2$
d
N
cm^{-3}
1.0
0.1
N_i
N_e
e
β
100
10
1
f
$Q^{1/2}$
0.4
0.2
0.0
$Q_i^{1/2}$
$Q_e^{1/2}$
05:26^{30}
05:26^{45}
05:27^{00}
05:27^{15}
Universal Time

Figure 7.

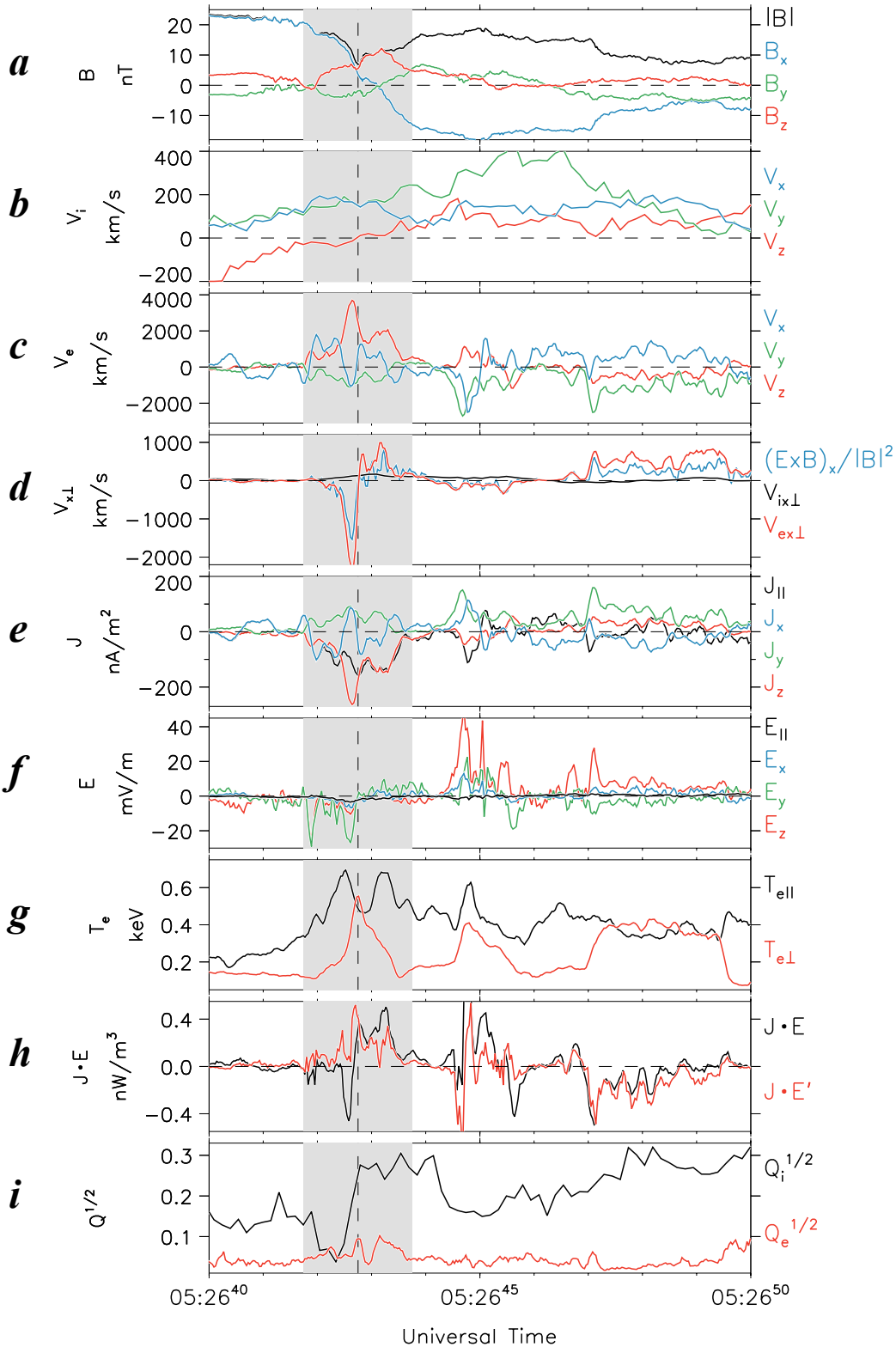
a
B
nT
20
10
0
−10
|B|
B_x
B_y
B_z
b
V_i
km/s
400
200
0
−200
V_x
V_y
V_z
c
V_e
km/s
4000
2000
0
−2000
V_x
V_y
V_z
d
$V_{x\perp}$
km/s
1000
0
−1000
−2000
$(ExB)_x/|B|^2$
$V_{ix\perp}$
$V_{ex\perp}$
e
J
nA/m²
200
0
−200
$J_{||}$
J_x
J_y
J_z
f
E
mV/m
40
20
0
−20
$E_{||}$
E_x
E_y
E_z
g
T_e
keV
0.6
0.4
0.2
$T_{e||}$
$T_{e\perp}$
h
J•E
nW/m³
0.4
0.0
−0.4
J•E
J•E′
i
$Q^{1/2}$
0.3
0.2
0.1
$Q_i^{1/2}$
$Q_e^{1/2}$
05:26⁴⁰
05:26⁴⁵
05:26⁵⁰
Universal Time

Figure 8.

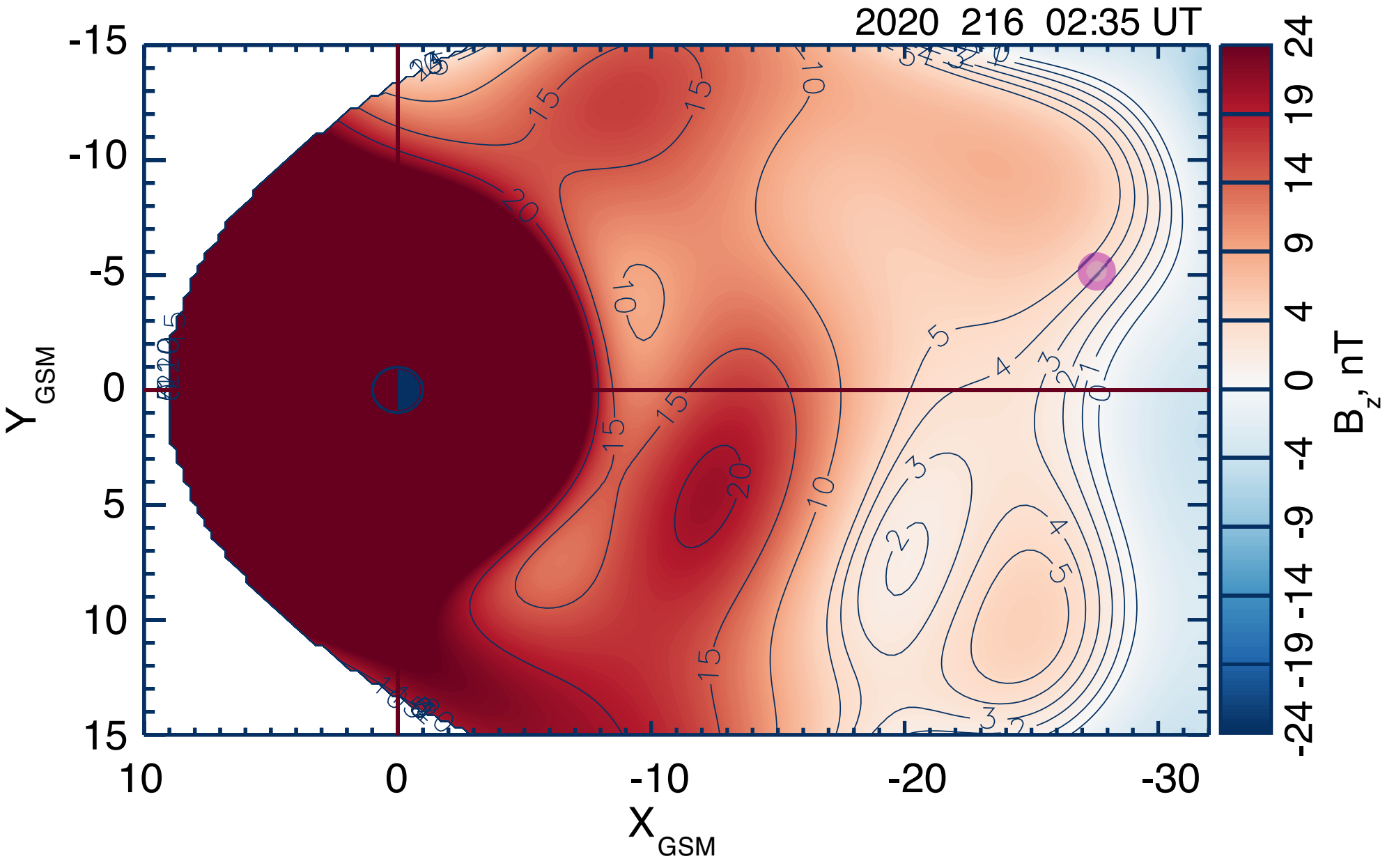
2020 216 02:35 UT
Y GSM
X GSM
B z, nT
-15
-10
-5
0
5
10
15
10
0
-10
-20
-30
24
19
14
9
4
0
-4
-9
-14
-19
-24

Figure 9.

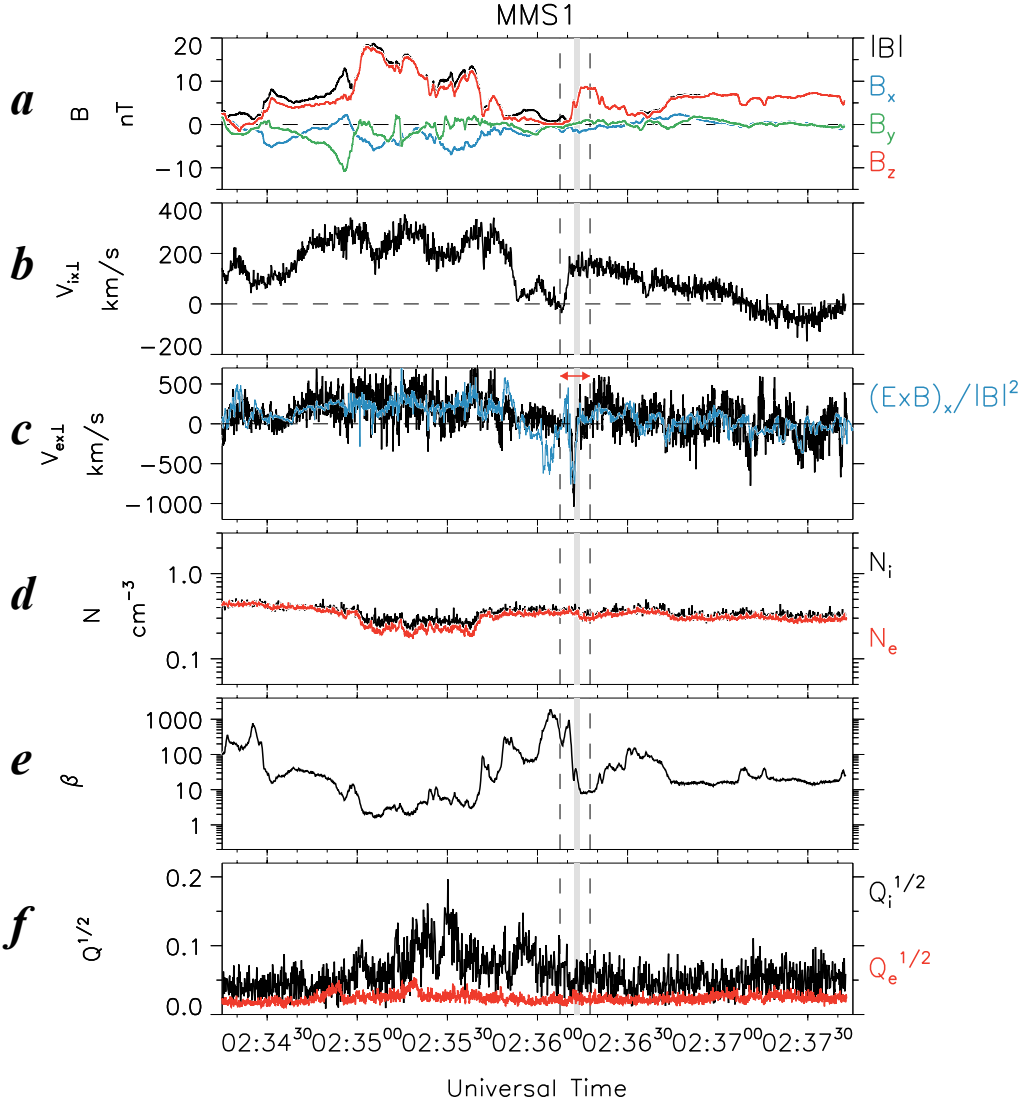
MMS1
a
B
nT
20
10
0
−10
|B|
B_x
B_y
B_z
b
$V_{ix\perp}$
km/s
400
200
0
−200
c
$V_{ex\perp}$
km/s
500
0
−500
−1000
$(ExB)_x/|B|^2$
d
N
cm^{-3}
1.0
0.1
N_i
N_e
e
β
1000
100
10
1
f
$Q^{1/2}$
0.2
0.1
0.0
$Q_i^{1/2}$
$Q_e^{1/2}$
02:34^{30} 02:35^{00} 02:35^{30} 02:36^{00} 02:36^{30} 02:37^{00} 02:37^{30}
Universal Time

Figure 10.

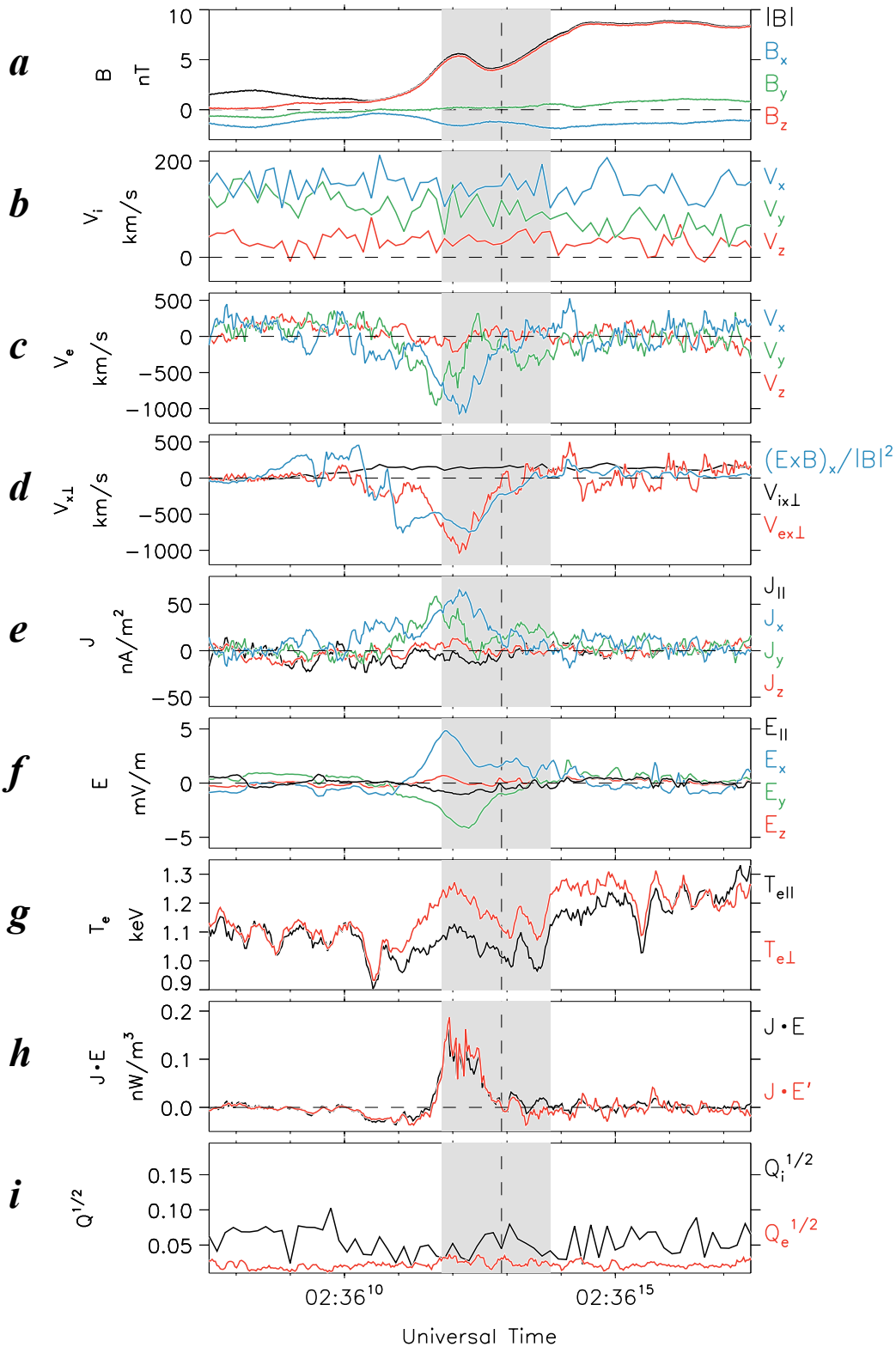
a
B
nT
10
5
0
|B|
B_x
B_y
B_z
b
V_i
km/s
200
0
V_x
V_y
V_z
c
V_e
km/s
500
0
−500
−1000
V_x
V_y
V_z
d
$V_{x\perp}$
km/s
500
0
−500
−1000
$(ExB)_x/|B|^2$
$V_{ix\perp}$
$V_{ex\perp}$
e
J
nA/m^2
50
0
−50
$J_{||}$
J_x
J_y
J_z
f
E
mV/m
5
0
−5
$E_{||}$
E_x
E_y
E_z
g
T_e
keV
1.3
1.2
1.1
1.0
0.9
$T_{e||}$
$T_{e\perp}$
h
J•E
nW/m^3
0.2
0.1
0.0
J • E
J • E′
i
$Q^{1/2}$
0.15
0.10
0.05
$Q_i^{1/2}$
$Q_e^{1/2}$
02:36^{10}
02:36^{15}
Universal Time

Figure 11.

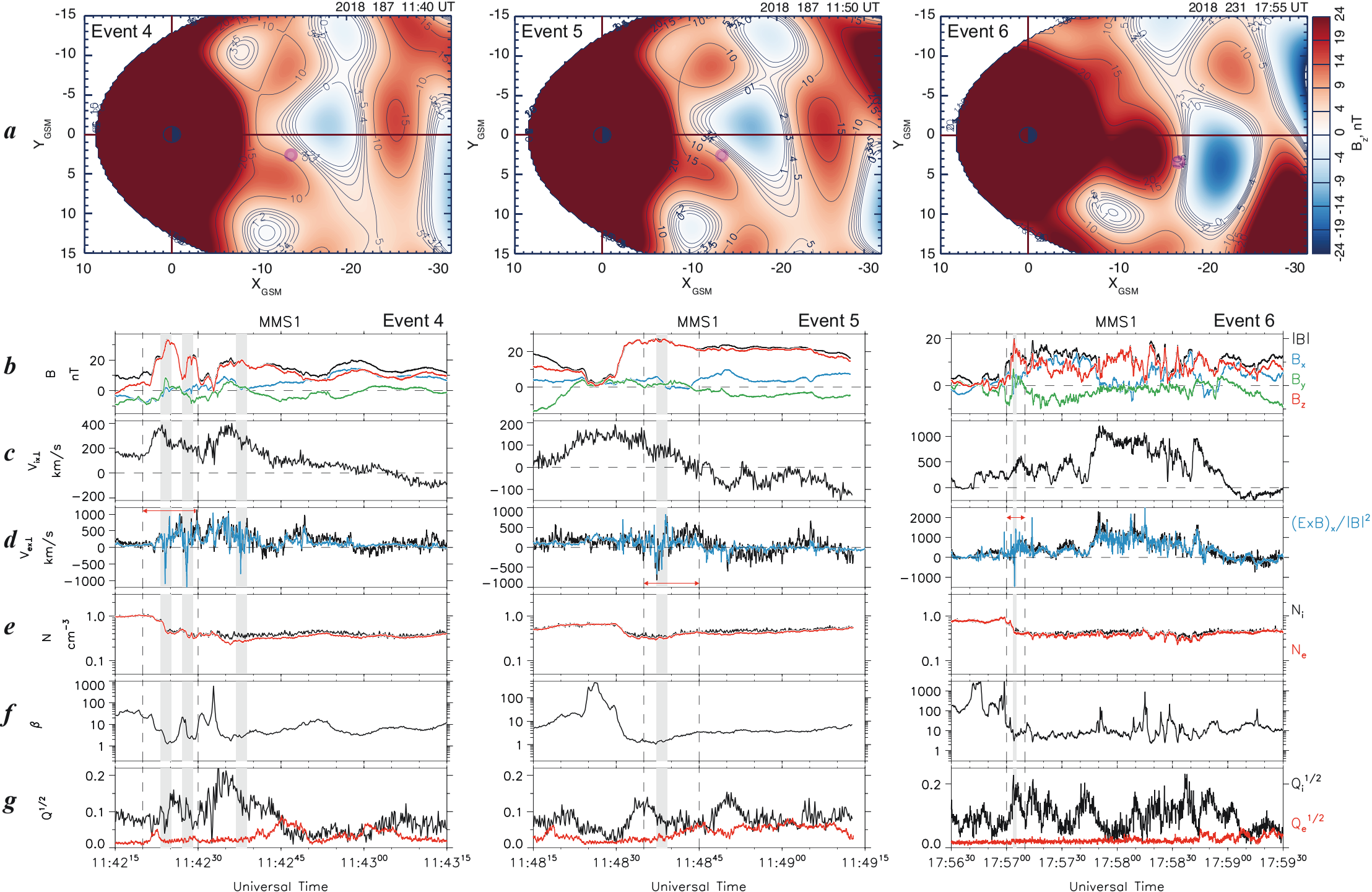
a
2018 187 11:40 UT
Event 4
2018 187 11:50 UT
Event 5
2018 231 17:55 UT
Event 6
Y GSM
X GSM
B, nT
b
c
d
e
f
g
MMS1
B
nT
$V_{ix\perp}$
km/s
$V_{ex\perp}$
km/s
N
cm^{-3}
β
$Q^{1/2}$
|B|
B_x
B_y
B_z
$(ExB)_x/|B|^2$
N_i
N_e
$Q_i^{1/2}$
$Q_e^{1/2}$
11:42^{15} 11:42^{30} 11:42^{45} 11:43^{00} 11:43^{15}
11:48^{15} 11:48^{30} 11:48^{45} 11:49^{00} 11:49^{15}
17:56^{30} 17:57^{00} 17:57^{30} 17:58^{00} 17:58^{30} 17:59^{00} 17:59^{30}
Universal Time